Acetylated dietary protein contributes to the acetylome in cells via KARS-mediated intra-translational deposition of acetyl-lysine in nascent protein

Dingyuan Guo[1]§, Xiaoyan Zhang[2]§, Jie He[1], Weixing Yu[1], Runxin Zhou[1], Fuqiang Tong[1], Sibi Yin[1], Yu Wang[1], Yuwen Yang[1], Xin Xu[3], Long Wang[3], Mingzhu Fan[4,5], Shan Feng[4,5], Changbao Hong[6], Chuixiu Huang[6], Ke Liu[7], Zhuqing Ouyang[2*], Yugang Wang[1,8,9*]

Affiliations:

[1]Department of Biochemistry and Molecular Biology, School of Basic Medicine, Tongji Medical College, Huazhong University of Science and Technology, Wuhan, Hubei, 430030, China. [2]Department of Pathogen Biology, School of Basic Medicine, Tongji Medical College, Huazhong University of Science and Technology, Wuhan, Hubei, 430030, China. [3]School of Chemistry and Chemical Engineering and Hubei Key Laboratory of Bioinorganic Chemistry and Materia Medica, Huazhong University of Science and Technology, Wuhan, Hubei, 430074, China. [4]Mass Spectrometry & Metabolomics Core Facility, The Biomedical Research Core Facility, Center for Research Equipment and Facilities, Westlake University, Hangzhou, Zhejiang, 310024, China. [5]Key Laboratory of Structural Biology of Zhejiang Province, School of Life Sciences, Westlake University, Hangzhou, Zhejiang, 310024, China. [6]Department of Forensic Medicine, School of Basic Medicine, Tongji Medical College, Huazhong University of Science and Technology, Wuhan, Hubei, 430030, China. [7] Department of Biostatistics, School of Public Health, Cheeloo College of Medicine, Shandong University, Jinan, 250000, China. [8]Cell Architecture Research Center, Huazhong University of Science and Technology, Wuhan, Hubei, 430030, China.

[9] Leading contact

§ These authors contribute equally

*Correspondence authors:

E-mail: zhuqingouyang@hust.edu.cn (Z.O.); yugangw@hust.edu.cn (Y.W.)

Abstract

N^6-acetyl-*L*-lysine residue is abundant in dietary protein but less is known about its potential influences on the diet-consumers. We herein report that N^6-acetyl-*L*-lysine residues in acetylated dietary protein directly contributes to the acetylome in animal. By feeding mice with deuterium-labelled N^6-acetyl-*L*-lysine-proteins, we demonstrated that acetylated dietary protein is a direct source of N^6-acetyl-*L*-lysine that can widely contribute the acetylome in organs of liver, brain, and lung in mice. In mammalian cells, N^6-acetyl-*L*-lysine can be utilized by Lysyl-tRNA synthetase (KARS) to generate N^6-acetyl-*L*-lysyl-tRNA, which introduces N^6-acetyl-*L*-lysine into the growing nascent polypeptide and intra-translationally results in protein acetylation. Co-crystal structure of KARS in complex with N^6-acetyl-*L*-lysyl-AMP and pyrophosphate, coupled with *in vitro* biochemical assays, further confirms a sequential mechanism that KARS produces N^6-acetyl-*L*-lysyl-AMP and transfers the N^6-acetyl-*L*-lysyl-moiety to lysine cognate tRNA to generate N^6-acetyl-*L*-lysyl-tRNA. Together, the present study establishes a model that N^6-acetyl-*L*-lysine bridges the influence of acetylated dietary protein to the acetylome in dietary protein-consumer. Importantly, an undocumented mechanism that intra-translationally deposit acetylation in nascent proteins has been proved. It might extend the repertoire of acetylome and improves our understandings in protein modification modes in cells.

Introduction

Lysine acetylation is a type of frequent and important protein post-translational modification (PTM) in biological system. In husbandry, lysine acetylation naturally occurs during the growth of animals and crops [1-3]. In food industry, it is intensively added to dietary proteins via chemical reactions, aiming to improve the physicochemical and functional properties of commercialized proteins [4-6]. As such, N^6-acetyl-*L*-lysine residues are abundant in dietary proteins. However, the influence of consuming acetylated proteins on biological system remains unclear. N^6-acetyl-*L*-lysine (AcK) is a theoretical product that derived from the digestion of acetylated proteins. It has been identified as a metabolite in mammals [7-9], but its functions are less studied. Whether and how N^6-acetyl-*L*-lysine residues in dietary protein contribute to the acetylome in dietary protein-consumer remain to be answered.

N^6-acetyl-*L*-lysine residues in diet contributes the acetylome of diet-consumer

To explore the cross-talk between the N^6-acetyl-*L*-lysine residues in dietary proteins and the ones in the acetylome of dietary protein-consumer, we produced and fed the deuterium-labelled acetylated protein (N^6-(acetyl-d_3)-*L*-lysine-protein) to mice and collected blood samples for performing high-performance liquid chromatography-tandem mass spectrometry (HPLC-MS/MS) analysis (Figure S1A and S1B). Identification of N^6-(acetyl-d_3)-*L*-lysine (d_3-AcK) in the blood samples built the connection between acetylated dietary protein and the metabolite of AcK in animal (Figure 1A and 1B; Figure S1C). To understand whether the diet-derived d_3-AcK could contribute to the acetylome in organs and tissues of mice, we collected the liver, brain, and lung from the studied mice and analyzed the acetylation profiles. Besides the non-labelled acetylation sites, we identified 867, 387, and 480 deuterium-labelled acetylation sites in liver, brain, and lung tissues, respectively (Figure 1C to 1E; Table

S1), revealing the contribution of diet-derived AcK to the acetylome in animal.

By analyzing the relative abundance of deuterium-labelled acetylation to the entire acetylation of specific lysine residues that were identified in both deuterium-labelled acetylome and non-labelled acetylome, we found about 28.6% of the acetylated lysine residues are majorly affected by deuterium-labelled acetylation (accounts more than 50% of the entire acetylation) (Figure 1F). The maximum contribution of deuterium-labelled acetylation to the entire acetylation of individual lysine residues reached 90.9% (Figure 1F; Table S2), indicating the substantial contribution of diet-derived AcK to the acetylation of certain lysine residues in the acetylome of protein consumer. We next performed biological processes enrichment analyses and found that deuterium-labelled acetylation occurs on 556 proteins that are enriched in 32 biological processes in the studied liver tissue (Figure S2; Table S3), 314 proteins that are enriched in 15 biological processes in the studied brain tissue (Figure S3; Table S3), and 333 proteins that are enriched in 9 biological processes in the studied lung tissue (Figure S4; Table S3). Most of the deuterium-labelled acetylation enriched biological processes and non-labelled acetylation enriched processes were overlapped, suggesting that food-derived AcK has wide influence on the acetylome and biological processes in animal. These results ascertain the model that N^6-acetyl-*L*-lysine bridges acetylated dietary protein and the acetylomes in dietary protein-consumer.

To understand how AcK contribute the acetylome in mammalian cells, we labelled the proteome of human liver cells with $^{13}C_6$,$^{15}N_2$-*L*-lysine and treated the labelled cells with deuterium-labelled AcK (N^6-(acetyl-d_3)-*L*-$^{12}C_6$,$^{14}N_2$-lysine, d_3-AcK) (Figure S1D and S1E). Proteomic analyses identified 274 N^6-(acetyl-d_3)-$^{13}C_6$,$^{15}N_2$-lysine-labelled acetylation sites, 1744 N^6-acetyl-$^{12}C_6$,$^{14}N_2$-lysine acetylation sites, and 215 N^6-(acetyl-d_3)-$^{12}C_6$,$^{14}N_2$-lysine-labelled acetylation sites (Figure 1G; Table S4), including the Lys-

34 and Lys-46/47 of histone H2B, Lys-118/119 and Lys-124 of histone H2A, and Lys-20 and Lys-26 of histone H1. Immunoblotting analysis validated that acetylation of these histone lysine residues can be upregulated by AcK (Figure S1F). Histone hyperacetylation might induce chromatin decondensation [10], which was observed in the AcK-treated cells (Figure S1G). These findings demonstrate the direct influence of AcK on the acetylome in cells. The combination of labelled and unlabeled acetyl-moisty and lysine residues indicate that the d_3-AcK might be converted into acetyl-moisty and *L*-lysine, which separately contribute the acetylome in cells [11]. This conversion might theoretical be a rapid enzymatic reaction. However, addition of N^6-(acetyl-d_3)-*L*-$^{12}C_6$,$^{14}N_2$-lysine (1mM) to the $^{13}C_6$,$^{15}N_2$-*L*-lysine (1mM) feeding cells did not significantly contribute intracellular *L*-$^{12}C_6$,$^{14}N_2$-lysine (Figure 1H), strongly suggesting that d_3-AcK is unlikely to be the source of *L*-lysine in the treated cells. As such, the hypothesis that d_3-AcK separately contribute d_3-acetyl-moisty and *L*-lysine to the proteome in cells was vetoed.

KARS can utilize N^6-acetyl-*L*-lysine to produce N^6-acetyl-*L*-lysyl-tRNA

To obtain purified recombinant proteins with site-specific lysine acetylation, Neumann et al established an *Escherichia coli* strain expressing modified lysyl-tRNA synthetase (KARS) that accommodates N^6-acetyl-*L*-lysine (AcK) in the catalytic pocket [12], allowing AcK being directly deposited into nascent polypeptides to produce proteins with acetylation. This system inspired us to propose another hypothesis that AcK could be directly incorporated into eukaryotic proteome. To test this hypothesis, we analyzed the structure of human wild-type KARS in complex with *L*-lysine and ATP (PDB ID: 3BJU) [13] and performed docking analysis. AcK fitted well in the substrate binding pocket and the predicted AcK-interacting residue profile was similar with that of lysine (Figure 2A to 2C), illustrating the possibility of AcK being a substrate of human wild-

type KARS. We next incubated purified KARS and tRNAs with AcK and observed ATP consumption and AMP production from the *in vitro* enzymatic assays (Figure 2D and 2E). The docking analyses illustrated that the residues of Glu301 and Arg323 interact with both AcK and lysine in the substrate binding pocket (Figure 2C). Replacement of these residues with alanine (KARS-E301A and KARS-R323A) significantly reduced both AcK and *L*-lysine dependent ATP consumption by KARS (Figure S5A and S5B). The Thr337 residue was predicted as the one that specifically mediate KARS interacting with AcK (Figure 2C). Replacement of Thr337 with alanine (KARS-T337A) significantly reduced the AcK-dependent ATP consumption by KARS while keeping its *L*-lysine-dependent ATP consumption activity intact (Figure S5A and S5B). Steady state kinetics analyses revealed that the maximum velocity (Vmax) and Michaelis Constant (K_m) of AcK-dependent KARS is 1.55±0.39 μM·minute^{-1} and 74.15±25.64 μM, respectively. Because KARS can catalyze the formation of *L*-lysyl-AMP that attacks the N^6-amino of *L*-lysine to generate *L*-lysyl-*L*-lysine and release AMP [14,15], we observed ATP consumption and AMP production by KARS in the absence of tRNAs (Figure S5C and S5D). As such, the Km and Vmax of the KARS-*L*-lysine and KARS-AcK assays cannot be precisely compared. However, we confirmed the activity of KARS utilizing AcK, tRNA, and ATP to produce AMP, which is similar with the reaction that KARS places on *L*-lysine.

L-lysyl-tRNA is the product of *L*-lysine dependent KARS catalysis. To test if KARS could perform similar reaction on AcK, we performed northern blotting assays following KARS-mediated *in vitro* reactions. The mobility shift of lysine cognate tRNAs in both the AcK and *L*-lysine dependent assays strongly suggest the abilities of KARS producing N^6-acetyl-*L*-lysyl-tRNAs by utilizing AcK (Figure 2F; Figure S5E),

shedding light on the possibility that KARS can utilize AcK to produce N^6-acetyl-*L*-lysyl-tRNAs.

To further understand how KARS utilizing AcK as substrate, we explored the molecular basis of KARS-catalyzed production of N^6-acetyl-*L*-lysyl-tRNA by crystalizing KARS (KARS-apo) and the complex obtained from the incubation of KARS, AcK, and ATP. Instead of the expected co-crystal of KARS in complex with AcK and ATP, we unexpectedly obtained the one representing KARS in complex with N^6-acetyl-*L*-lysyl-AMP and pyrophosphate (KARS-AcK-AMP, 2.26 Å, deposited in PDB, PDB ID: 8HYQ) (Figure 3A; Table S6). Compared to the sequential mechanism that KARS generates *L*-lysyl-AMP, transfers the *L*-lysyl-moiety to tRNAs, and release *L*-lysyl-tRNAs (Figure 3B) [16], the co-crystal structure of KARS-AcK-AMP demonstrates that KARS can perform similar reaction on AcK and produce N^6-acetyl-*L*-lysyl-AMP. The aminoacyl-tRNA that was generated from the incubation of KARS and AcK is therefore confirmed as N^6-acetyl-*L*-lysyl-tRNA (Figure 2F).

The structures of KARS-apo (2.55 Å, deposited in PDB, PDB ID: 8HYR) (Figure S6A), KARS-AcK (Figure 3C), and KARS-AcK-AMP (Figure 3A) represent the states of KARS in standby, substrates binding, and products releasing, respectively. To understand the dynamicity of KARS in catalyzing the production of N^6-acetyl-*L*-lysyl-tRNA, we analyzed the superimposition of KARS-apo and KARS-K and found a compacted catalytic domain while KARS accommodating *L*-lysine (Figure S6B). The compacted catalytic domain might facilitate the interaction between substrates for catalytic reaction (Figure S6B) [17]. Similar conformational change was observed in the structure of KARS-AcK (Figure 3C), illustrating similar structural dynamics while KARS utilizing AcK as substrate. By analyzing the superimposition of KARS-AcK (substrates-binding) and KARS-AcK-AMP (products-releasing) (Figure 3D), we found

the catalytic pocket of KARS becomes loosen. The helices of α-10, α-12, α-13, α-15, and α-16, as well as the sheets of β-13 and β-14, around the catalytic pocket were pushed outward to create an enlarged channel, which might allow the relocation of the AcK from the substrates binding position to the products releasing position (Figure S6C), along with the newly conjugated AMP moiety in the form as N^6-acetyl-*L*-lysyl-AMP. The helix η and its associated loop (η+L) that originally cover the substrates are invisible in the KARS-AcK-AMP structure (Figure 3D), indicating flexibility of these regions so that they can be pushed aside to facilitate the release of N^6-acetyl-*L*-lysyl-AMP. Interactions between pyrophosphate and the residues of Gln467 and Arg507 at the edge of the catalytic domain were observed (Figure 3E and 3F). These interactions might provide driving force for the release of pyrophosphate. Mutation of Gln467 and Arg507 (KARS-Q467A and KARS-R507A) significantly reduced the catalysis of the KARS-AcK reaction but the KARS-*L*-lysine reaction is unexpectedly intact (Figure S6D and S6E), suggesting a different pyrophosphate-releasing mechanism is used by KARS-K reaction [18]. A water molecule neighboring the pyrophosphate was observed (Figure 3E). It might provide additional driving forces for pyrophosphate releasing. From substrates-binding to products-releasing, the structural dynamicity majorly occurs in the aminoacylation catalytic domain while keeping the tRNA binding domain intact (Figure S6F), suggesting limited influences of KARS-catalyzed N^6-acetyl-*L*-lysyl-AMP production on its interaction with tRNAs. As such, generation of N^6-acetyl-*L*-lysyl-AMP is the determinant step to produce N^6-acetyl-*L*-lysyl-tRNA. These structural analyses, together with the enzymatic activity studies, lead to the conclusion that KARS can naturally utilize AcK to generate N^6-acetyl-*L*-lysyl-tRNA.

KARS-produced N^6-acetyl-*L*-lysyl-tRNA results in deposition of N^6-acetyl-*L*-lysine in nascent proteins

KARS-catalyzed *L*-lysyl-tRNA is an intermediary introducing *L*-lysine into growing nascent polypeptides in protein synthesis. N^6-acetyl-*L*-lysyl-tRNA is likely to have similar role that introduces N^6-acetyl-*L*-lysine into growing polypeptides and generate nascent proteins bearing acetylated-lysine residues. Besides the above results, this hypothesis was also supported by the result that AcK dose-dependently upregulated acetylation of protein that was synthesized in a mammalian cell-free protein expression system (Figure 4A). Because of the direct deposition of AcK in nascent proteins, N^6-(acetyl-d_3)-*L*-$^{12}C_6$,$^{14}N_2$-lysine sites were identified in the d_3-AcK-treated $^{13}C_6$,$^{15}N_2$-*L*-lysine-labelled cells (Figure 1G and 4B); because the deuterium-labelled acetyl-moisty can be removed by deacetylase and leave the *L*-$^{12}C_6$,$^{14}N_2$-lysine residues that can be re-acetylated by PTM mechanisms [11,19], the N^6-acetyl-$^{12}C_6$,$^{14}N_2$-lysine sites were identified (Figure 1G and 4B); the removed acetyl-moisty could be recycled as d_3-acetyl-CoA that can be utilized in acetylation of other lysine residues [20,21], so that N^6-(acetyl-d_3)-$^{13}C_6$,$^{15}N_2$-lysine sites were identified (Figure 1G and 4B); degradation of both N^6-(acetyl-d_3)-*L*-$^{12}C_6$,$^{14}N_2$-lysine and N^6-acetyl-$^{12}C_6$,$^{14}N_2$-lysine bearing proteins can release the nonlabelled-lysine, so that the delayed identification of lysine in the d_3-AcK treated $^{13}C_6$,$^{15}N_2$-*L*-lysine-labelled cells (Figure 1H and 4B). Notable amount of deuterium-labelled acetylation sites localizing inside the buried regions of proteins were identified in the studied acetylomes (Table S5), such as retinal dehydrogenase (ALDH1A1, protein ID: P24549, Lys113 and Lys193) and cytoplasmic isocitrate dehydrogenase (IDH1, protein ID: O88844, Lys72) (Figure 4C to 4E). These acetylated sites are inaccessible to the acetyltransferases, which are required for protein acetylation via PTM-mechanism. Because direct incorporation of AcK during the growth of nascent polypeptide occurs prior to the folding of proteins, it makes acetylation of these buried lysine residues possible. These evidences collectively lead

to the conclusion that KARS-mediated incorporation of AcK in nascent protein naturally occurs in mammal, resulting in acetyltransferases-independent protein acetylation.

Taken together, the present study demonstrates that N^6-acetyl-*L*-lysine directly bridges the N^6-acetyl-*L*-lysine residues in dietary protein and the acetylomes in dietary protein-consumer. Direct incorporation of AcK into nascent proteins is an undocumented and important mechanism that AcK contribute the acetylome in cells. KARS can utilize N^6-acetyl-*L*-lysine to produce N^6-acetyl-*L*-lysyl-tRNA, which introduces AcK into nascent polypeptide synthesis, resulting in protein acetylation prior to the accomplishment of protein synthesis (Figure 4F). Compared with the well-known PTM mechanisms that occur after protein synthesis [22], this undocumented mechanism leads to protein acetylation in the middle of protein translation, it is therefore termed as intra-translational modification (ITM). ITM-acetylation naturally and widely occurs in multiple organs. It provides us with new understandings in the mechanisms for protein modification and extends the repertoire of acetylome in cells.

Discussion

While the direct contribution of N^6-acetyl-*L*-lysine to the acetylome in mammalian system has been demonstrated in the present study, it is premature to state the physiological influence of daily consumption of acetylated dietary protein. In the present study, we noted that AcK treatment showed limited influence on the level of pan-acetylation in cells (Figure S7A). We believe these negative responses came from the monitor of deacetylases that remove "unfavorable" acetylation to ensure the acetylome couples with the physiological state of cells [23,24]. Without the deacetylases-dependent surveillance, AcK could increase the level of pan-acetylation in cells (Figure S7B). Although studies are expected to explain how deacetylases sense and remove the

diet-derived impacts on intracellular acetylome, the potential influences of acetylated dietary protein on the patients taking deacetylase inhibitors need to be monitored.

ITM-acetylation is an undocumented protein modification mechanism that co-translationally occurs and installs acetylation prior to the accomplishment of protein synthesis, so that any lysine residues in the proteome, including the one localized in the buried and PTM-inaccessible regions, can theoretically be modified by ITM-acetylation. Modification of the buried residues might disturb the inter-residue interactions inside proteins and influence the functions of the affected proteins [25]. For instance, Lys113 and Lys193 are buried inside the structure of ALDH1A1 (Figure 4C and 4D) [26]. Acetylation can neutralize the positive charge of Lys113 and Lys193 that might disrupt their interactions with Asp122 and Glu196 (Figure 4C and 4D), respectively. We expressed and purified the proteins of ALDH1A1 wide-type and acetylation mimic mutants (ALDH1A1-K113Q and ALDH1A1-K193Q) (Figure S8A). Acetylation-mimic mutation of Lys113 and Lys193 significantly disrupted the enzymatic activity of ALDH1A1 (Figure S8B). Thermofluor shift assays revealed lower Tm of the ALDH1A1-K193Q mutant than that of wide-type (Figure S8C), suggesting ITM-acetylation of Lys193 disrupts the stability of ALDH1A1 protein. Acetylation of Lys72 of IDH1 is another illustrative example. We expressed and purified the proteins of IDH1 wide-type and acetylation mimic mutant IDH1-K72Q (Figure S8D). Steady kinetic studies revealed that IDH1-K72Q has higher Km (95.22±54.67 μM) toward NADP than that of wild-type IDH1 (16.45±5.97 μM) (Figure S8E). The maximum velocity (Vmax) of utilizing NADP to produce NADPH by IDH1-K72Q (2.43±0.45 $\mu M \cdot minute^{-1}$) is significantly lower than its wide-type counterpart (11.52±1.53 $\mu M \cdot minute^{-1}$) (Figure S8F and S8G). We therefore conclude that the acetylation-mimic mutation could disrupt the binding of IDH1 to NADP and reduce the enzymatic activity. Moreover, IDH1-

K72Q mutant showed lower thermo-stability than IDH1wide-type in thermofluor shift assays (Figure S8H), suggesting ITM-acetylation on the buried Lys72 residue could reduce the stability of IDH1. Physical interaction between deacetylases and acetylated substrates is also required for protein deacetylation, so that the acetylated residues in the PTM-cold regions might escape from the surveillance of deacetylases. As such, it is worthy asking the accumulative effect of acetylation in the buried regions of proteins on cells.

ITM-acetylation provides us a new mode for protein modification that might be parallel with PTM-mechanism. There are at least three facets to be refined to sculpture the outline of ITM-acetylation. First, mechanisms regulating ITM-acetylation remains elusive. Second, besides buried lysine residues, lysine residues on the surface of proteins can also be acetylated by ITM mechanism. Because deacetylases and acetyltransferases can mix the ITM-acetylome and PTM-acetylome by exchanging the acetyl-moisty between lysine residues, so that, even in the isotope-labelled system, it is technically hard to tell whether a certain lysine acetylation is deposited by ITM or PTM mechanism. However, it is important to understand the cross-talk between ITM-acetylation and PTM-acetylation. Third, only small number of ITM-acetylation sites were identified in the PTM-cold regions, suggesting that ITM-acetylation in PTM-cold regions are monitored by mechanisms that remain to be explored. Besides acetylation, other types of protein modification are also likely to be installed by ITM mechanism. Relevant reports are expected to diversify the field of protein intra-translational modification in future.

Reference

1 Li, X. *et al.* Effects of protein posttranslational modifications on meat quality: A review.

Compr Rev Food Sci F **20**, 289-331, doi:10.1111/1541-4337.12668 (2021).
2 Smith-Hammond, C. L., Swatek, K. N., Johnston, M. L., Thelen, J. J. & Miernyk, J. A. Initial description of the developing soybean seed protein Lys-N(epsilon)-acetylome. *J Proteomics* **96**, 56-66, doi:10.1016/j.jprot.2013.10.038 (2014).
3 Jiang, S., Liu, Y., Shen, Z., Zhou, B. & Shen, Q. W. Acetylome profiling reveals extensive involvement of lysine acetylation in the conversion of muscle to meat. *J Proteomics* **205**, 103412, doi:10.1016/j.jprot.2019.103412 (2019).
4 Miedzianka, J., Zambrowicz, A., Zielinska-Dawidziak, M., Drozdz, W. & Nems, A. Effect of Acetylation on Physicochemical and Functional Properties of Commercial Pumpkin Protein Concentrate. *Molecules* **26**, doi:10.3390/molecules26061575 (2021).
5 Miedzianka, J., Peksa, A. & Aniolowska, M. Properties of acetylated potato protein preparations. *Food Chem* **133**, 1283-1291, doi:10.1016/j.foodchem.2011.08.080 (2012).
6 Jaiswal, A. K. *Food processing technologies : impact on product attributes*. (CRC Press, 2017).
7 Zierer, J. *et al.* The fecal metabolome as a functional readout of the gut microbiome. *Nat Genet* **50**, 790-+, doi:10.1038/s41588-018-0135-7 (2018).
8 Gonzalez-Dominguez, R., Jauregui, O., Queipo-Ortuno, M. I. & Andres-Lacueva, C. Characterization of the Human Exposome by a Comprehensive and Quantitative Large-Scale Multianalyte Metabolomics Platform. *Anal Chem* **92**, 13767-13775, doi:10.1021/acs.analchem.0c02008 (2020).
9 Dallmann, R., Viola, A. U., Tarokh, L., Cajochen, C. & Brown, S. A. The human circadian metabolome. *P Natl Acad Sci USA* **109**, 2625-2629, doi:10.1073/pnas.1114410109 (2012).
10 Zhang, J. J. *et al.* Nuclear dihydroxyacetone phosphate signals nutrient sufficiency and cell cycle phase to global histone acetylation. *Nat Metab* **3**, 859-875, doi:10.1038/s42255-021-00405-8 (2021).
11 Paik, W. K., Bloch-Frankenthal, L., Birnbaum, S. M., Winitz, M. & Greenstein, J. P. ϵ-Lysine acylase. *Arch Biochem Biophys* **69**, 56-66, doi:10.1016/0003-9861(57)90472-1 (1957).
12 Neumann, H., Peak-Chew, S. Y. & Chin, J. W. Genetically encoding N-epsilon-acetyllysine in recombinant proteins. *Nat Chem Biol* **4**, 232-234, doi:DOI 10.1038/nchembio.73 (2008).
13 Guo, M., Ignatov, M., Musier-Forsyth, K., Schimmel, P. & Yang, X. L. Crystal structure of tetrameric form of human lysyl-tRNA synthetase: Implications for multisynthetase complex formation. *P Natl Acad Sci USA* **105**, 2331-2336, doi:10.1073/pnas.0712072105 (2008).
14 He, X. D. *et al.* Sensing and Transmitting Intracellular Amino Acid Signals through Reversible Lysine Aminoacylations. *Cell Metab* **27**, 151-+, doi:10.1016/j.cmet.2017.10.015 (2018).
15 Yanagisawa, T., Sumida, T., Ishii, R., Takemoto, C. & Yokoyama, S. A paralog of lysyl-tRNA synthetase aminoacylates a conserved lysine residue in translation elongation factor P. *Nat Struct Mol Biol* **17**, 1136-U1114, doi:10.1038/nsmb.1889 (2010).
16 Ling, J., Reynolds, N. & Ibba, M. Aminoacyl-tRNA synthesis and translational quality control. *Annu Rev Microbiol* **63**, 61-78, doi:10.1146/annurev.micro.091208.073210 (2009).
17 Guo, Y., Li, D. F., Ji, H. N., Zheng, J. T. & Zhou, N. Y. Hexachlorobenzene Monooxygenase Substrate Selectivity and Catalysis: Structural and Biochemical Insights. *Appl Environ Microb* **87**, doi:ARTN e01965-20
10.1128/AEM.01965-20 (2021).
18 Desogus, G., Todone, F., Brick, P. & Onesti, S. Active site of lysyl-tRNA synthetase: Structural studies of the adenylation reaction. *Biochemistry-Us* **39**, 8418-8425, doi:10.1021/bi0006722 (2000).
19 Wolfson, N. A., Pitcairn, C. A., Sullivan, E. D., Joseph, C. G. & Fierke, C. A. An enzyme-coupled assay measuring acetate production for profiling histone deacetylase specificity. *Anal Biochem* **456**, 61-69, doi:10.1016/j.ab.2014.03.012 (2014).

20 Fujino, T., Kondo, J., Ishikawa, M., Morikawa, K. & Yamamoto, T. T. Acetyl-CoA synthetase 2, a mitochondrial matrix enzyme involved in the oxidation of acetate. *J Biol Chem* **276**, 11420-11426, doi:DOI 10.1074/jbc.M008782200 (2001).
21 Luong, A., Hannah, V. C., Brown, M. S. & Goldstein, J. L. Molecular characterization of human acetyl-CoA synthetase, an enzyme regulated by sterol regulatory element-binding proteins. *J Biol Chem* **275**, 26458-26466, doi:DOI 10.1074/jbc.M004160200 (2000).
22 Drazic, A., Myklebust, L. M., Ree, R. & Arnesen, T. The world of protein acetylation. *Bba-Proteins Proteom* **1864**, 1372-1401, doi:10.1016/j.bbapap.2016.06.007 (2016).
23 Narita, T., Weinert, B. T. & Choudhary, C. Functions and mechanisms of non-histone protein acetylation. *Nat Rev Mol Cell Bio* **20**, 156-174, doi:10.1038/s41580-018-0081-3 (2019).
24 Sabari, B. R., Zhang, D., Allis, C. D. & Zhao, Y. M. Metabolic regulation of gene expression through histone acylations. *Nat Rev Mol Cell Bio* **18**, 90-101, doi:10.1038/nrm.2016.140 (2017).
25 Gromiha, M. M. & Selvaraj, S. Inter-residue interactions in protein folding and stability. *Prog Biophys Mol Bio* **86**, 235-277, doi:10.1016/j.pbiomolbio.2003.09.003 (2004).
26 Xiaoyan Zhang, Z. O. Crystal structure of aldehyde dehydrogenase 1A1 from mouse. *Biochem Bioph Res Co*, doi:https://doi.org/10.1016/j.bbrc.2022.08.054 (2022).
27 Baeza, J. *et al.* Stoichiometry of Site-specific Lysine Acetylation in an Entire Proteome. *J Biol Chem* **289**, 21326-21338, doi:10.1074/jbc.M114.581843 (2014).

Acknowledgements

We sincerely thank Dr. Hongtao Yu at the Westlake University for his scientific input in this work. We thank the staff from BL18U1 beamline of National Facility for Protein Science in Shanghai (NFPS) at Shanghai synchrotron Radiation Facility, for assistance during data collection. This work was supported by National Natural Science Foundation of China (91957110 and 31970577 to Y.W, 31870751 to Z.O), the National Key Research and Development Program of China (2018YFE0204500 to Z.O).

Author Contributions

Y.W. and Z.O conceived and designed the study and wrote the manuscript. D.G., X.Z., W.Y., Y.W., F.T., S.Y., and S.L. performed the biochemical experiments to identify the KARS activities *in vivo* and *in vitro*. J.H., C.H., and C.H., performed HPLC-MS/MS to quantitatively analyze N^6-acetyl-*L*-lysine and *L*-lysine in cells and blood samples. R.Z. and K.L. performed bioinformatics analyses. X.X. and L.W performed the chemical synthesis of N^6-(acetyl-d_3)-*L*-lysine. M.F. and S.F. performed proteomic analyses. X.Z. and Z.O. performed structural analyses.

Author Information: The authors declare no competing financial interests.

Figure legends

Figure 1. N^6-acetyl-*L*-lysine residues in diet contributes the acetylome of diet-consumer.

(**A**), Identification of N^6-(acetyl-d_3)-*L*-lysine in the blood of mice fed with N^6-(acetyl-d_3)-*L*-lysine-protein. N^6-(acetyl-d_3)-*L*-lysine in the blood samples and chemical synthesized N^6-(acetyl-d_3)-*L*-lysine show similar elution time in the same HPLC-MS/MS system.

(**B**), The kinetics of N^6-(acetyl-d_3)-*L*-lysine and lysine in the blood of mice fed with N^6-(acetyl-d_3)-*L*-lysine-protein and control protein, respectively. Each data is presented as the means±s.d. of five mice (n=5).

(**C**) to (**E**), Analyses of the acetylome of organs in the mice fed with N^6-(acetyl-d_3)-*L*-lysine-protein. The N^6-(acetyl-d_3)-modified lysine residues are ITM-acetylation sites. The N^6-acetyl-modified lysine residues are PTM-acetylation sites. The ITM-acetylation sites and PTM-acetylation sites that were identified in the liver (**C**), brain (**D**), and lung (**E**) are represented, respectively.

(**F**), Quantitative analysis of the contribution of ITM-acetylation to the entire acetylation of individual lysine residues. To avoid the biases inherent in the use of antibody-based enrichment methods that employed prior to the proteomic analysis [27], only the pairs of ITM-acetylated peptides and PTM-acetylation peptides with the same features (length, amino acid sequence, modifications and modification sites) were used for the quantitative analyses. Details for calculating the contribution of ITM-acetylation to the entire acetylation of each lysine residues are described in the part of **materials and methods**.

(**G**), Identification of the N^6-(acetyl-d_3)-*L*-lysine residues in the $6C_{13}$,$2N_{15}$-*L*-lysine-

labelled cells. The left panel shows the scheme of N^6-(acetyl-d_3)-*L*-lysine incorporating in the $6C_{13}$,$2N_{15}$-*L*-lysine-labelled proteome. The right panel shows the scheme of the HPLC-MS/MS identified peptides that are resulted from the direct incorporation of N^6-(acetyl-d_3)-*L*-lysine in $6C_{13}$,$2N_{15}$-*L*-lysine-labelled proteins and the PTM-resulted protein acetylation in the $6C_{13}$,$2N_{15}$-*L*-lysine-labelled cells. The number of identified acetylation positions are presented. The detail information about the identified acetylation positions is listed in the supplementary table S5.

(**H**), Quantification of N^6-(acetyl-d_3)-*L*-lysine and *L*-lysine in cells. Kinetic studies of N^6-(acetyl-d_3)-*L*-lysine and *L*-lysine in $^{13}C_6$,$^{15}N_2$-*L*-lysine-labelled cells treated with N^6-(acetyl-d_3)-*L*-lysine. The cells were cultured in the medium suppled with 1 mM $^{13}C_6$,$^{15}N_2$-*L*-lysine. Each data is presented as the means±s.d. of three assays (n=3).

Figure 2. KARS can utilize N^6-acetyl-*L*-lysine to produce N^6-acetyl-*L*-lysyl-tRNA

(**A**) to (**C**), N^6-acetyl-*L*-lysine can be accommodated in the substrate binding pocket of KARS. The substrate-binding pocket of human KARS structure (PDB code: 3BJU) (**A**) was referred to perform the docking structure of KARS in complex with N^6-acetyl-*L*-lysine (AcK) (**B**). *L*-lysine and N^6-acetyl-*L*-lysine are shown as sticks. The residues that interact with *L*-lysine and N^6-acetyl-*L*-lysine are shown as sticks, labeled in the zoomed-in view of the substrate-binding pocket of human KARS, and listed (**C**), respectively.

(**D**) and (**E**), KARS can utilize N^6-acetyl-*L*-lysine to catalyze the conversion of ATP into AMP. Purified KARS was incubated with ATP, N^6-acetyl-*L*-lysine, and tRNAs for 1 hour. The ATP consumption (**D**) and AMP production (**E**) in the assays were measured and quantitatively analyzed. Two-sided *t*-test analyses were conducted. The data is presented as the means±s.d. of three independent experiments (n=3). $^*P<0.05$.

(**F**), KARS catalyzes the formation of aminoacyl-tRNAs by using lysine and N^6-acetyl-*L*-lysine, respectively. Northern blotting analysis of lysine cognate tRNAs by using fluorescence-labelled single strand DNA probe that specifically recognizes lysine cognate tRNAs. The free lysine cognate tRNA and aminoacyl-tRNAs are indicated with black and red arrows, respectively. Representative images of triplicate experiments are shown.

Figure 3. The molecular basis of KARS utilizing N^6-acetyl-*L*-lysine as substrate.

(**A**), Co-crystal structure of KARS in complex with N^6-acetyl-*L*-lysyl-AMP and pyrophosphate. Cartoon drawing of KARS-AcK-AMP structure with zoomed in view of N^6-acetyl-*L*-lysyl-AMP and pyrophosphate. The ligands are shown as sticks, along with their 2*Fo*-*Fc* electron density map (blue mesh) contoured at 1.0 σ.

(**B**), The scheme of the molecular process of KARS catalyzing the production of *L*-lysyl-tRNA by using *L*-lysine. KARS catalyzes the specific attachment of L-lysine to its cognate tRNA in a 2-step reaction. L-lysine is first activated by ATP to form L-lysyl-AMP and pyrophosphate is a byproduct of this step. Then the L-lysyl-moiety is transferred from *L*-lysyl-AMP to lysine cognate tRNA to form L-lysyl-tRNA.

(**C**), Structural difference between KARS in the states of standby and substrate-binding. Superimposition the structures of KARS-apo and KARS-AcK is performed. Only the regions showing structural difference between the KARS-apo (green) and KARS-AcK (cyan) are colored and labelled, including the helixes of α-10, α-12, α-13, α-15, and α-16, the helix η and its associated loop (η+L), and the sheets of β-13, β-14, and β-15. N^6-acetyl-*L*-Lysine is shown as sticks.

(**D**), Structural difference between KARS in the states of substrate-binding and products-releasing. Superimposition the structures of KARS-AcK and KARS-AcK-AMP is performed. Only the regions showing structural difference between the KARS-AcK (cyan) and KARS-AcK-AMP (red) are colored and labelled, including the helixes of α-10, α-12, α-13, α-15, and α-16, the helix η and its associated loop (η+L), and the sheets of β-13 and β-14. The compounds of N^6-acetyl-*L*-Lysine, N^6-acetyl-*L*-lysyl-AMP, and pyrophosphate are removed for better illustration of the protein structures.

(**E**), Zoomed-in view of the pyrophosphate-binding site of KARS-AcK-AMP structure. Pyrophosphate-binding residues are shown as sticks and labeled. The ordered water molecule (W) and the values of the distance (green dash line) are also indicated.

(**F**), Surface drawing of the crystal structure of KARS-AcK-AMP in two different orientations. N^6-acetyl-*L*-lysyl-AMP and pyrophosphate are shown in sticks. Pyrophosphate-binding residues are colored in yellow.

Figure 4. N^6-acetyl-*L*-lysyl-tRNA results in deposition of N^6-acetyl-*L*-lysine in nascent proteins.

(**A**), N^6-acetyl-*L*-lysine results in acetylation of the protein that is synthesized by cell-free protein expression system. The influence of N^6-acetyl-*L*-lysine on protein synthesis was studied by the gradient addition of N^6-acetyl-*L*-lysine in a mammalian cell-free protein expression system. The synthesized protein and its acetylation level were analyzed by performing immunoblotting assays with the indicated antibodies. Representative images of triplicate experiments are shown.

(**B**), Scheme of the pathways for the stable isotope labelled and non-labelled acetyl-moisty and L-lysine exchange in the studied acetylomes.

(**C**) and (**D**), Zoomed in and transparent view of mouse ALDH1A1 structure (PDB code: 7YOB). The acetylated Lys113 residue (**C**) and Lys193 residue (**D**) that localize in the buried regions of ALDH1A1 are illustrated. The acetylation affected lysine residues are shown as sticks and highlighted in red. The negative charged Asp122 and Glu196 that interact with Lys113 and Lys193 are shown as sticks and highlighted in blue, respectively.

(**E**), Zoomed in and transparent view of mouse IDH1 structure (PDB code: 5YZH). The acetylated Lys72 residue that localizes in the buried regions of IDH1 is shown as sticks and highlighted in red. The substrate NADP is highlighted in blue.

(**F**), Scheme of the KARS-mediated intra-translational deposition of acetyl-lysine in nascent protein results in protein acetylation.

Supplementary Figure Legends

Figure S1. N^6-acetyl-*L*-lysine residues in diet contributes the acetylome of diet-consumer.

(**A**), Illustration of the workflow of synthesizing deuterium-labelled acetylated dietary protein (N^6-(acetyl-d_3)-*L*-lysine-protein).

(**B**), Validation of the synthesized deuterium-labelled acetylated dietary protein by performing immunoblotting assay with the antibody against acetyl-lysine. Representative images of triplicate experiments are shown.

(**C**), Identification of N^6-(acetyl-d_3)-*L*-lysine in the blood from mice fed with N^6-(acetyl-d_3)-*L*-lysine-protein. The parent ion and other two ion fragments of synthesized N^6-(acetyl-d_3)-*L*-lysine have similar elution profiles with that of N^6-(acetyl-d_3)-*L*-lysine-lysine that identified in the blood from mice fed with N^6-(acetyl-d_3)-*L*-lysine-protein.

(**D**), Illustration of the workflow of synthesizing deuterium-labelled N^6-acetyl-*L*-lysine (N^6-(acetyl-d_3)-*L*-lysine).

(**E**), Validation of the synthesized N^6-(acetyl-d_3)-*L*-lysine. ^{1}H NMR (D_2O, 500 MHz, 295 K, ppm) spectrum of the synthesized N^6-(acetyl-d_3)-*L*-lysine, recorded on the Agilent spectrometer.

(**F**), N^6-acetyl-*L*-lysine treatment upregulates acetylation of core histones. The cultured LO2 cells were treated with 1 mM N^6-acetyl-*L*-lysine for a series of time-points. The acetylation level of histone H2A K118 and histone H2B K46 in the treated cells were analyzed by immunoblotting assays with the indicated antibodies. Representative images of triplicate experiments are shown.

(**G**), N^6-acetyl-*L*-lysine treatment induced decondensation of chromatin in cells. The

nuclei were isolated from cultured cells that had been treated with 5mM N6-acetyl-L-lysine for a series of time-points. The nuclei were then incubated with MNase, by which the genomic DNA in the decondensated chromatin regions was digested. The genomic DNA with and without MNase digestion was separated in 1.5% DNA electrophoresis agarose gel and visualized by DNA dye staining. Representative images of triplicate experiments are shown.

Figure S2 Biological processes enriched with proteins with ITM-acetylation in mice liver.

Nodes stand for KEGG defined pathways ($P<0.001$ and FDR<0.001). Each node represents one biological process. The node size reflects the number of proteins in the pathway. Two nodes are connected if there were one or more proteins included in both nodes. Biological processes that are enriched by PTM-acetylated proteins (red), ITM-acetylated proteins (cyan), and proteins in both ITM-acetylome and PTM-acetylomes (plum) are highlighted in colors.

Figure S3. Biological processes enriched with proteins with ITM-acetylation in mice brain.

Nodes stand for KEGG defined pathways ($P<0.001$ and FDR<0.001). Each node represents one biological process. The node size reflects the number of proteins in the pathway. Two nodes are connected if there were one or more proteins included in both nodes. Biological processes that are enriched by PTM-acetylated proteins (red), ITM-acetylated proteins (cyan), and proteins in both ITM-acetylome and PTM-acetylomes (plum) are highlighted in colors.

Figure S4. Biological processes enriched with proteins with ITM-acetylation in mice lung.

Nodes stand for KEGG defined pathways (P<0.001 and FDR<0.001). Each node represents one biological process. The node size reflects the number of proteins in the pathway. Two nodes are connected if there were one or more proteins included in both nodes. Biological processes that are enriched by PTM-acetylated proteins (red), ITM-acetylated proteins (cyan), and proteins in both ITM-acetylome and PTM-acetylomes (plum) are highlighted in colors.

Figure S5. KARS can utilize N^6-acetyl-*L*-lysine to produce N^6-acetyl-*L*-lysyl-tRNA

(**A**) and (**B**) Identification of N^6-acetyl-*L*-lysine and lysine interacting residues in the substrate binding pocket of KARS. Purified wild-type KARS and its mutants were incubated with ATP, tRNAs, and N^6-acetyl-*L*-lysine (**A**) or *L*-lysine (**B**) or for 1 hour. The ATP consumption in the assays were measured and quantitatively analyzed. Two-sided *t*-test analyses were conducted. The data is presented as the means±s.d. of three independent experiments (n=3). $^{**}P<0.01$.

(**C**) and (**D**), KARS can catalyze ATP consumption and AMP production in the absence of tRNAs. Purified KARS was incubated with ATP and *L*-lysine for 1 hour. The ATP consumption (**C**) and AMP production (**D**) in the assays were measured and quantitatively analyzed. Two-sided *t*-test analyses were conducted. The data is presented as the means±s.d. of three independent experiments (n=3). $^{**}P<0.01$.

(**E**), KARS-E301A mutant losses the activity of catalyzing the formation of aminoacyl-tRNAs by using *L*-lysine and N^6-acetyl-*L*-lysine. Northern blotting analysis of lysine cognate tRNAs by using fluorescence-labelled single strand DNA probe that specifically recognizes lysine cognate tRNAs. Representative images of triplicate experiments are shown.

Figure S6. The molecular basis of KARS utilizing N^6-acetyl-*L*-lysine as substrate.

(**A**), Crystal structure of KARS-apo. Cartoon drawing of KARS-apo structure.

(**B**), Structural difference between KARS in the states of standby and *L*-lysine-binding. Superimposition the structures of KARS-apo and KARS-K is performed. Only the regions showing structural difference between the KARS-apo (green) and KARS-K (blue) are colored and labelled, including the helixes of α-10, α-12, α-13, and α-15, the helix η and its associated loop (η+L), and the sheets of β-13, β-14, and β-15. *L*-Lysine and ATP are shown as sticks.

(**C**), Surface drawing of the structures of KARS in the states of substrate-binding (KARS-AcK, left) and products-releasing (KARS-AcK-AMP, right). AcK, N^6-acetyl-*L*-lysyl-AMP, and pyrophosphate are shown in sticks.

(**D**) and (**E**), Gln467 and Arg507 are important to the N^6-acetyl-*L*-lysine-dependent KARS activity. The Gln467 and Arg507 are mutated to Alanine, respectively. The in vitro KARS activity assays showed that Gln467 and Arg507 mutations significantly reduce N^6-acetyl-*L*-lysine-dependent KARS activity (**D**) but have no influence on the lysine-dependent KARS activity (**E**). Each data is presented as the means±s.d. of three assays (n=3). Two-sided *t*-test analyses were conducted. $^{**}P<0.01$.

(**F**), Structure alignments of KARS-apo, KARS-AcK, and KARS-AcK-AMP. Superimposition the structures of KARS-apo, KARS-AcK, and KARS-AcK-AMP is performed. Only the regions showing structural difference between the KARS-apo (green), KARS-AcK (cyan), and KARS-AcK-AMP (red) are colored and labelled, including the helixes of α-10, α-12, α-13, α-15, and α-16, the helix η and its associated loop (η+L), and the sheets of β-13, β-14, and β-15. The compounds of N^6-acetyl-*L*-

Lysine, N^6-acetyl-*L*-lysyl-AMP, and pyrophosphate are removed for better illustration of the protein structures.

Figure S7. Deacetylases might surveil the influence of N^6-acetyl-*L*-lysine on the acetylome in cells.

(**A**), N^6-acetyl-*L*-lysine treatment has no influence on the *pan*-acetylation of proteome in cells. The cultured LO2 cells were treated with 1 mM N^6-acetyl-*L*-lysine for a series of time-points. The *pan*-acetylation of proteins in the treated cells were analyzed by immunoblotting assays with the indicated antibodies. Representative images of triplicate experiments are shown.

(**B**), N^6-acetyl-*L*-lysine treatment increases the *pan*-acetylation of proteins in cells treated with deacetylase inhibitor cocktail. The cultured LO2 cells were treated with 1 mM N^6-acetyl-*L*-lysine for a series of time-points. Deacetylase inhibitor cocktail is added in the experiments to avoid the surveillance of deacetylases that might possibly remove the AcK treatment-induced protein acetylation in cells. The *pan*-acetylation of proteins in the treated cells were analyzed by immunoblotting assays with the indicated antibodies. Representative images of triplicate experiments are shown.

Figure S8. ITM can deposit acetylation in the PTM-cold regions of proteins.

(**A**), Coomassie blue staining shows the purified protein of ALDH1A1wide-type and ALDH1A1 ITM-acetylation mimic mutants (ALDH1A1 K113Q and ALDH1A1 K193Q, respectively).

(**B**), Acetylation mimic mutations of Lys113 and Lys193 reduce activity of ALDH1A1. The enzymatic activity assays of ALDH1A1 wide-type and mutants are performed by measuring the NADH production in each assay. Each data is presented as the means±s.d. of three independent assays (n=3).

(**C**), Acetylation mimic mutation of Lys193 reduce the thermostability of ALDH1A1. The temperature of melting of ALDH1A1 wide-type and mutants are measured by thermofluor shift assays. Each data is presented as the means±s.d. of four independent assays (n=4).

(**D**), Coomassie blue staining shows the purified protein of IDH1 wide-type and ITM-acetylation mimic mutant (IDH1 K72Q).

(**E**) and (**F**), Acetylation mimic mutation of Lys72 reduces the NADP-binding ability and enzymatic activity of IDH1. The Michaelis Constant (Km) (**E**) and maximum velocity (Vmax) (**F**) of IDH1 utilizing NADP to produce NADPH were calculated through the steady kinetics analysis of IDH1. Each data is presented as the means±s.d. of three assays (n=3). Two-sided *t*-test analyses were conducted. *$P<0.05$, **$P<0.01$.

(**G**) Acetylation mimic mutation of Lys72 reduces the activity of IDH1. The enzymatic activity assays of IDH1 wide-type and mutants are performed by measuring the NADPH production in each assay. Each data is presented as the means±s.d. of three independent assays (n=3).

(**H**) Acetylation mimic mutation of Lys72 reduces the thermostability of IDH1. The temperatures of melting of IDH1 wide-type and IDH1 K72Q are measured by performing thermofluor shift assays. Each data is presented as the means±s.d. of four independent assays (n=4).

Materials and Methods

Materials

Primary antibodies for immunoblotting: β-actin (mouse, Cat#AC004, lot#3500100006, Abclonal, Wuhan, China), Acetylation-lysine (rabbit, Cat#9441S, lot#15, Cell Signaling Technology, MA, USA), Luciferase (rabbit, Cat#A18259, lot#3501634001, Abclonal, Wuhan, China). The SILAC DMEM medium (Cat#88425) were purchased from Thermo fisher (Shanghai, China) and prepared according to the manufacturer's guideline. Fluorescent probe for detecting lysine cognate tRNA probe (5'Cy5.5-ATT AAG AGT CAT ACG CG) was synthesized and purchased from Sangon Biotech (Shanghai, China). Nucleic acid gel stain Solargreen (Cat#G5570) was purchased from Solarbio (Beijing, China). Northern blot hybridization solution (Cat#AM8663) and nylon membrane (Cat#AM10100) were purchased from Thermo Fisher Scientific (Shanghai, China). Diethyl Pyrocarbonate (Cat#V900882) and tRNA from brewer′s yeast (Cat#10109525001) were purchased from Sigma-Aldrich (Shanghai, China). N^6-acetyl-*L*-lysine (Cat#N159376) were purchased from Aladdin (Aladdin, Shanghai, China). Six-week-old female ICR and C57BL/J were purchased from Hubei Bainte Biological Technology Co., Ltd.

Cell culture and stable isotope labeling

Human hepatocyte LO2 cells were kindly provided by Dr. Weidong Xie at Tsinghua University. The cells were cultured in Dulbecco's modified Eagle's medium (Cat#SH30285.01, Cytiva Life Sciences, MA, USA) supplemented with 10% fetal bovine serum (Cat#086-150, WISENTINC, Quebec, Canada) and 1% penicillin and streptomycin (Cat#BL505A, biosharp, Beijing, China). The cultured cells were kept at 37°C in the cell culture incubator (CLM-170B-8-NF, ESCO, Singapore) with 5% CO_2.

To label the proteome of cultured cells, cells were labeled and maintained in SILAC DMEM medium that was supplemented with 1mM $^{13}C_6{}^{15}N_2$-*L*-lysine (Cat#608041, Sigma-Aldrich, Shanghai, China), 10% dialyzed fetal bovine serum, and 1% penicillin and streptomycin. After ten cell doublings, the labelling efficiency was more than 99.5%.

Synthesis of N^6-(acetyl-d_3)-*L*-lysine

To obtain N^6-(acetyl-d_3)-*L*-lysine, *L*-Lysine was first dissolved in $NaHCO_3$ aqueous solution. To the given solution, $CuSO_4 \cdot 5H_2O$ in water and $NaHCO_3$ were added. The mixture was cooled to 0 °C by ice bath and acetic anhydride-d_6 (Cat#175641, Sigma-Aldrich, Shanghai, China) was added dropwise. After stirred at room temperature for 12 h, a pale blue suspension was formed. After filtration, the pale blue solid was suspended in water, then 8-hydroxyquinoline was added. The suspension was stirred for 10 h, and the color changed from blue to yellow. After filtration, the filtrate was washed with ethyl acetate. The aqueous phase was freeze-dried to give the with solid product (yield: 28%). The products were identified by the ^{1}H NMR spectrum.

Acetylation of soy proteins

The acetylation of soy proteins was performed according to the protocol that was previously reported [28]. Briefly, soy protein (Cat#9010-10-0, Shanghai Macklin Biochemical Co., Ltd, Shanghai, China) was homogenized with 0.1M carbonate buffer, pH 8.3, for 3 h at room temperature. Acetic anhydride-d_6 (Cat#175641, Sigma-Aldrich, St. Louis, USA) was gradually added to the soy protein isolate solution (anhydride/protein = 0.6-1g/g) and carried out for 1h. The solution pH was adjusted with 2.5M NaOH to be in the range of 8.0-8.5. After the pH has stabilized, the solution was kept at room temperature for 2h, and then dialyzed with double-distilled water at

4°C for 48h to remove excess anhydride. The dialyzed protein was freeze-dried and stored at -20°C.

Acetyl-peptide enrichment and identification

The $^{13}C_6{}^{15}N_2$-*L*-lysine-labelled LO2 cells (>6×10^8) were treated with 10mM N^6-(acetyl-d_3)-*L*-lysine for 48h. Then the cells were collected and washed three times with ice-cold PBS. Mice were daily fed with 0.1g N^6-(acetyl-d_3)-*L*-lysine-protein for 5 days. Organs and tissues were collected and washed three times with ice-cold PBS and stored at -80°C for later analysis.

Collected cells or tissue samples (>0.2g each) were lysed and homogenized with urea lysis buffer (20 mM HEPES pH 8.0, 9 M urea, 1×protease and phosphatase inhibitor cocktail, 1×deacetylase Inhibitor Cocktail). Lysates were sonicated (60-Watt output with 6 bursts of 10 sec each, ice-bath for 30 sec between each burst) to shear genomic DNA. The protein concentrations were determined using BCA protein assay kit. 20 mg protein from each sample was processed for further procduces.

Acetylated peptides were enriched following the PTMScan kit (Cell Signaling Technologies, Danvers, MA, USA) protocol with some modifications. Briefly, proteins were reduced with 5 mM dithiothreital at room temperature for 60 min followed by alkylation with 20 mM iodoacetamide in dark for 30 minutes at room temperature. Proteins were diluted 4-fold with 20 mM HEPES pH 8.0 and then digested with trypsin at the enzyme-to-substrate ratio of 1:75 overnight at room temperature with gentle mixing. Peptides from the digestion reactions were desalted using Oasis HLB cartridge and lyophilized. To enrich acetyl-peptides, incubating the sample with PTMScan® acetyl-lysine motif immunoaffinity beads overnight at 4°C. The beads were washed twice with immunoaffinity purification buffer and three times with mass spectrometry

grade water. Then the enriched acetyl-peptides were eluted with 100 ul of 0.15% TFA and lyophilized.

Identification of acetyl-peptides by LC-MS/MS. The enriched acetyl-peptides were analyzed with the Thermo EASY-nLC1200 integrated nano-HPLC system that was directly interfaced with the Thermo Q Exactive HF-X mass spectrometer. Peptides in the chromatographic system were eluted with solvent A (0.1% formic acid) and solvent B (80% acetonitrile and 0.1% formic acid) at a flow rate of 0.300 μL/min. Each sample was analyzed nine times (6.5μL of the sample per run). The mass spectrometer was operated in the data-dependent acquisition mode using the Xcalibur 4.1 software. There is a single full-scan mass spectrum in the Orbitrap (400-1800 m/z, 60,000 resolution) that was followed by 20 data-dependent MS/MS scans at 30% normalized collision energy. Each mass spectrum was analyzed using the Thermo Xcalibur Qual Browser and Proteome Discoverer for the database searching.

Quantitative analysis of ITM-acetylation was only performed by using the pairs of ITM-acetylated peptides and PTM-acetylation peptides with the same features (length, amino acid sequence, modifications and modification sites). The contribution of ITM-acetylation to the entire acetylation of each lysine residues was calculated by using the equation $c = \frac{AI}{AI+AP}$, where c presents contribution of ITM-acetylation to the entire acetylation of each lysine residues, *AI* presents the abundance of the ITM-acetylated peptide that calculated in the MS system, AP presents the abundance of the PTM-acetylated peptide that has the same profile with that of ITM-acetylated peptide.

Quantitative analysis of N^6-(acetyl-d_3)-*L*-lysine in serum

Blood samples were collected from mice fed with 0.05g N^6-(acetyl-d_3)-*L*-lysine-protein or control proteins (without acetylation treatment). The blood samples were

collected from mouse's retro-orbital sinus at the indicated time-points. The serum was isolated by centrifuging the blood at 3000rpm for 15min. 50μl serum was obtained at each time-point from each mouse. The metabolites were extracted twice with 80% methanol in water. Two extracts from the same sample were combined and dried by Vacufuge Concentrator System (Eppendorf 5301, Eppendorf, Germany).

The amino acids in mice serum were quantitatively analyzed using LC-MS/MS. 50μl of methanol/water (1:4, v/v) was applied for reconstitution. The final reconstitution samples (injection volume: 2μl) were injected into a 100×4.6mm 3.5 μm high-performance liquid chromatography column (XBridgeTM Amide, Waters, USA). The mobile phase A was consisted of 5 mM ammonium acetate in 0.1% formic acid solution, and mobile phase B was methanol organic phases. Data acquisition was performed using an Ultimate 3000 HPLC system interfaced with a TSQ Quantum Access MAX triple quadrupole Mass Spectrometry (Thermo Fisher Scientific, Waltham, MA, USA).

Quantitative analysis of N^6-(acetyl-d_3)-*L*-lysine in LO_2 cell

To analyze the intracellular concentration of N^6-(acetyl-d_3)-*L*-lysine, the cultured cells were treated with 1mM N^6-(acetyl-d_3)-*L*-lysine and collected at the indicated time-points. The collected cells were washed three times with ice-cold PBS. The metabolites were extracted with 80% methanol in water and collected following 15,000 rpm×20 minutes centrifuge. The metabolites were included in the supernatant that was dried by Vacufuge Concentrator System (Eppendorf 5301, Eppendorf, Germany). The final reconstitution samples were injected into a 100×4.6mm 3.5 μm high-performance liquid chromatography column (XBridgeTM Amide, Waters, USA). The mobile phase consisted of ammonium acetate and formic acid in both aqueous and organic phases. Data acquisition was performed using a UHPLC–LTQ/Orbitrap MS (Thermo Fisher

Scientific, Waltham, MA, USA) via an Ion Trap Orbitrap positive ion mode.

Plasmids, protein expression and purification

The $KARS_{70–580}$ gene was cloned into pET-20b vector with C-terminal 6×His tag and overexpressed in *Escherichia coli* BL-21 strain. Protein expression was induced with 0.2 mM isopropyl β-D-1-thiogalactopyranoside (IPTG) at 16°C for 20 h. Then the bacteria were harvested and resuspended in lysis buffer (20 mM Tris-HCl pH 8.0, 350 mM NaCl, 20mM imidazole, 1 mM PMSF, 1 mM benzamidine and 10 mM β-Me). The cells were lysed by "JNBIO" Low Temperature Ultra-High-Pressure Continuous Flow Cell Disrupter (JN-Mini Pro, JNBIO, Guangzhou, China) and the soluble supernatant was collected by centrifugation at 25000 g for 1 h at 4°C. The supernatant was passed through a gravity column with 2 mL Ni Focurose 6FF IMAC (HZ1003-5, HUIYAN Bio, Wuhan, China) that had previously been equilibrated with lysis buffer. Protein was then purified using a Resource™ Q 6ml column (17-1179-01, GE Healthcare, Uppsala, Sweden) and a Superdex 200 Increase 10/300 column (28-9909-44, GE Healthcare, Uppsala, Sweden) equilibrated with 25 mM HEPES pH 7.5, 150 mM NaCl and 5 mM DTT. The peak fractions containing the protein were pooled and concentrated in centrifugal concentrators (CLVG01230, Merck Millipore, Cork, Ireland) to a final concentration of 30 mg/ml for crystallization. Plasmids expressing KARS-R323A, KARS-T337A, KARS-Q467A and KARS-R507A were made by site-directed mutagenesis.

The mouse IDH1 and ALDH1A1 gene were cloned into a pColdI expression vector with *N*-terminal hexahistidine tag separately and overexpressed in *Escherichia coli* T7 Express cell line (BC206-01, Biomed, Beijing, China). Protein expression was induced with 0.2 mM isopropyl β-D-1-thiogalactopyranoside at 16°C for 20 h. Then the bacteria were harvested and protein was purified with Ni Focurose 6FF IMAC (HZ1003-5,

HUIYAN Bio, Wuhan, China) and eluted with elution buffer 2 (20 mM Tris-HCl, pH 7.5, 500 mM NaCl, 300mM imidazole, pH8.0, 10% glycerol, 5 mM β-Me). Then the protein was concentrated with centrifugal concentrators (UFC901096, Merck Millipore, Cork, Ireland), and loaded onto a Superose^{TM} 6 Increase 10/300 GL gel-filtration column (29-0915-96, GE Healthcare, Uppsala, Sweden) equilibrated with 20 mM HEPES, pH 7.5, 200 mM NaCl, 2mM DTT, 10% glycerol. The purity of the fractions containing the protein was checked by SDS-PAGE analysis. Acetylation-mimic mutants of K72Q, K113Q and K193Q were made by site-directed mutagenesis.

Recombinant protein activity assays

KARS activity assays were performed according to the protocol that was previously described [29]. Briefly, the reaction mixture containing 30 mM Tris-Cl pH 7.5, 150 mM NaCl, 30 mM KCl, 40 mM MgCl2, 1 mM DTT, 10 μM ATP, 3 mg/ml tRNA and 10 mM lysine or N^6-acetyl-*L*-lysine were started by adding 20 μg KARS (WT/Q467A/R507A/E301A/R323A/T337A). Enzymatic activities of KARS wide-type and mutants were determined by measuring AMP production and ATP consumption with AMP-Glo Assay Kit (Cat#V5011, Promega, Madison, USA) and ATP Bioluminescent Assay Kit (Cat#FLAA, Sigma-Aldrich, Shanghai, China) or ATP Assay Kit (Cat#S0026, Beyotime, Shanghai, China), respectively.

IDH1 activity assays were performed according to the protocol that was previously reported [30]. Briefly, the reaction mixture containing 20 mM Tris-Cl, pH 7.5, 150 mM NaCl, 10 mM $MgCl_2$, 0.05% BSA, 2 mM β-Me, 4ng IDH1 WT/K72Q, 0.35 mM isocitrate were started by adding 0.25 μM NADP+. The IDH1-produced NADPH was measured by the diaphorase/resazurin system, which converts resazurin into resorufin (excitation 550 nm, emission 585 nm) that was quantitatively analyzed by plate reader (CLARIOstar Plus, BMG Labtech, German).

ALDH1A1 activity assays were performed according to the protocol that was previously reported [30]. Briefly, the reaction mixture containing 50 mM Tris-Cl, pH 7.5, 200 mM NaCl, 10 mM KCl, 2 mM DTT, 200 ng ALDH1A1 WT/K113Q/K193Q, 1 mM acetaldehyde were started by adding 250 μM NAD+. The ALDH1A1-produced NADH was measured by the diaphorase/resazurin system, which converts resazurin into resorufin (excitation 550 nm, emission 585 nm) that was quantitatively analyzed by plate reader (CLARIOstar Plus, BMG Labtech, German). The concentrations of recombinant proteins were determined by Pierce™ Rapid Gold BCA Protein Assay Kit (Cat#A53225, Thermo Fisher Scientific, Rockford, USA).

Thermofluor Shift Assay

SYPRO Orange Protein Gel Stain (Cat#S5692, Sigma-Aldrich, St. Louis, USA) were diluted 1:2500 into the assay buffer (150 mM NaCl, 200 mM Tris-Cl pH 7.5, 10 mM MgCl2, 20 mM β-Mercaptoethanol). ALDH1A1 (WT/Mutant) or IDH1 (WT/Mutant) was added with the final concentration of 0.2 μM, respectively. The 50 μl mixture were loaded into PCR 8-Strip Tubes (Cat#CP0101, GSBIO, Wuxi, China). Melting curves were obtained applying a temperature gradient from 25 to 99 °C and a heating rate of 0.5 °C/s. The fluorescence intensity was measured by a CFX Connect™ Real-Time PCR System (Cat#1855201, Bio-Rad, USA).

Crystallization, Data Collection and Structure Determination

To obtain the co-crystal of KARS70–580 binding to N^6-acetyl-*L*-lysine (AcK), protein solution of $KARS_{70–580}$ was first preincubated with synthetic AcK ($nKARS_{70–580}$: nAcK=1:10) and 5 mM ATP for 1 h at 4°C. The initial crystallization screening was carried out by the sitting-drop vapor-diffusion method at 16°C using commercial screening kits. Crystals were observed after 7-8 days in a condition containing 0.06 M

Morpheus Divalents, 0.1 M Morpheus Buffer system 1, pH 6.5 and 30% Morpheus Precipitant Mix 2. Single crystals were obtained by the seeding method. Crystals were harvested and subsequently soaked in mother liquor supplemented with 5 mM AcK and 5 mM ATP for approximately 11 hours. The crystals were cryoprotected with the reservoir solution supplemented with 20% (v/v) glycerol and then flash-cooled in liquid nitrogen. The space group of the crystal is $P2_12_12_1$, with cell dimensions of a = 130 Å, b = 90 Å, and c = 107 Å. There are two molecules in the asymmetric unit with a 53% solvent content. $KARS_{70–580}$ apo form crystals were obtained in a similar condition.

X-ray diffraction data were collected from a single crystal on beamline BL17U1 and BL18U1 of National Facility for Protein Science in Shanghai (NFPS) synchrotron Radiation Facility and processed with XDS and AIMLESS[31]. The structure of $KARS_{70–580}$-AcK complex was determined and refined using the phenix suite program[32]. The structure of human LysRS (PDB entry 3bju) was processed by the Sculptor program. Two ensembles, one containing residue 300-430 and the other comprising the rest part in chain A of 3bju, were used for MR search. Model building was performed using Coot[33]. Model refinement was carried out with Phenix-Refine[34]. Ramachandran plot and the quality of the structure were evaluated with MolProbity [35]. The final models were deposited in the protein Data Bank with accession code 7VWQ (KARS-apo) and 7VWR (KARS-AcK). PyMOL was used to present the structure. Refinement statistics are summarized in Table S6.

Structure docking analysis

Molecular docking of N^6-acetyl-*L*-lysine with $KARS_{70–580}$ was performed using CB-Dock (http://cao.labshare.cn/cb-dock/), a web server used for predicting ligand-protein interaction blindly with a popular docking program [36]. The result with the highest docking scores was used for structure analysis.

MNase assay

Chromatin decondensation was tested as previously described (reference #13 in the manuscript). Nuclei extractions were performed by using the Nuclei PURE Prep kit (Cat#NUC201, Sigma-Aldrich, Shanghai, China). For MNase assay, 5μl nuclei were digested with micrococcal nuclease (Cat#M0247S, NEB, MA, USA) at 37℃ for gradient time. The digestion was stopped by adding 0.5M EDTA (pH 8.0). To analyze the digested genomic DNA, proteinase K(NEB) and RNase A (Solarbio) were added in the digestion products which were incubated at 37°C for 1hour to remove protein and RNA. Genomic DNA were purified using phenol–chloroform extraction and then analyzed by 1.5% agarose gel.

Analysis of the surface accessibility of ITM-acetylation exclusive sites

By using the protein ID in the ITM-exclusive acetylome, we found the link of the structure in the UniProt database (https://www.uniprot.org/), then obtained the PDB format structure files of the candidate proteins from the PDB database (https://www.rcsb.org/). The spatial position of the candidate lysine sites in the candidate proteins were analyzed by using Swiss-PdbViewer 4.1.0 software. If the accessibility of the lysine residues to the surface is less than 30%, it can be termed as buried inside, otherwise it was termed as outside. If the structure is not available in PDB, a homolog protein structure with high identity will be analyzed, or we analyze the burying status of the candidate lysine residues by using alphafold predicted structure (https://alphafold.ebi.ac.uk/).

Immunoblotting

Proteins were extracted from cultured cell using 0.5% SDS lysis buffer containing protease, deacetylase and phosphatase inhibitor cocktail. Immunoblotting analyses with

indicated antibodies were performed as described previously [37].

Cell Free Protein Expression Coupled with N^6-acetyl-*L*-lysine

The cell free protein expression assays were performed by using the TnT® Quick Coupled Transcription/Translation System (Cat#L1171, Promega, Madison, USA), according to the manufacturer's guideline with minor modification. Briefly, the DNA template for luciferase expression is the positive control DNA template that is provided in the kit. Gradient titrations of N^6-acetyl-*L*-lysine were added in the assays. The incubation condition for protein synthesis is 30°C for 2hr. The protein expression level of luciferase is detected by immunoblotting assay with the antibody against luciferase (rabbit, Cat#A18259, lot# 3501634001, Abclonal, Wuhan, China). The acetylation level of the synthesized luciferase was measured by immunoblotting assay with the antibody against pan-acetylation lysine.

Analysis of *L*-lysyl-tRNA and N^6-acetyl-*L*-lysyl-tRNA by northern blot hybridization

KARS-catalyzed reactions were performed by mxing 10 mM Lysine or N^6-acetyl-*L*-lysine, 1 mM ATP, 3 mg/ml tRNA and 40 μg KARS that were incubated at 37°C for 2h. The produced *L*-lysyl-tRNA and N^6-acetyl-*L*-lysyl-tRNA were separated from total tRNAs with acid-urea polyacrylamide gel electrophoresis and detected with the method that was previously described [38]. Briefly, 4 μg of total tRNA mix sample was loaded to a 12% gel. The electrophoreses were performed with100 V constant voltage at 4 °C for 8.5 hours. The tRNA was transferred onto nylon membrane by TRANS-Blot SD (Cat#170-3940, Bio-Rad, USA) at 650 mA for 30 min and the membrane was washed briefly in 5 × SSC (0.75 M sodium chloride, 0.075 M sodium citrate, adjust to pH 7.0 with 1 N HCl) and cross-linked by UV using 120mJ. The membrane was hybridized

overnight with Cy5.5 labelled tRNA probe at 30℃. The signal was scanned and collected by an Odyssey CLX for fluorescence detection after membrane was washed by washing buffer (6 × SSC, 0.1% SDS) for twice.

Pathway Enrichment

Kyoto Encyclopedia of Genes and Genomes (KEGG) pathway enrichment analysis was performed via DAVID (https://david.ncifcrf.gov/), and data was visualized using the Enrichment Map v3.3.3 [39] and yFiles Layout Algorithms v1.1.1 plugin of Cytoscape v3.8.2 [40].

Statistical Analysis

The significance of differences in the experimental data was determined using Student's *t*-test (two-tailed) unless specifically indicated. Differences in means were considered statistically significant at $P < 0.05$ or $P < 0.01$.

Supplemental Reference

1 Li, X. *et al.* Effects of protein posttranslational modifications on meat quality: A review. *Compr Rev Food Sci F* **20**, 289-331, doi:10.1111/1541-4337.12668 (2021).

2 Smith-Hammond, C. L., Swatek, K. N., Johnston, M. L., Thelen, J. J. & Miernyk, J. A. Initial description of the developing soybean seed protein Lys-N(epsilon)-acetylome. *J Proteomics* **96**, 56-66, doi:10.1016/j.jprot.2013.10.038 (2014).

3 Jiang, S., Liu, Y., Shen, Z., Zhou, B. & Shen, Q. W. Acetylome profiling reveals extensive involvement of lysine acetylation in the conversion of muscle to meat. *J Proteomics* **205**, 103412, doi:10.1016/j.jprot.2019.103412 (2019).

4 Miedzianka, J., Zambrowicz, A., Zielinska-Dawidziak, M., Drozdz, W. & Nems, A. Effect of Acetylation on Physicochemical and Functional Properties of Commercial Pumpkin Protein Concentrate. *Molecules* **26**, doi:10.3390/molecules26061575 (2021).

5 Miedzianka, J., Peksa, A. & Aniolowska, M. Properties of acetylated potato protein preparations. *Food Chem* **133**, 1283-1291, doi:10.1016/j.foodchem.2011.08.080 (2012).

6 Jaiswal, A. K. *Food processing technologies : impact on product attributes*. (CRC Press, 2017).

7 Zierer, J. *et al.* The fecal metabolome as a functional readout of the gut microbiome. *Nat Genet* **50**, 790-+, doi:10.1038/s41588-018-0135-7 (2018).

8 Gonzalez-Dominguez, R., Jauregui, O., Queipo-Ortuno, M. I. & Andres-Lacueva, C. Characterization of the Human Exposome by a Comprehensive and Quantitative Large-Scale Multianalyte Metabolomics Platform. *Anal Chem* **92**, 13767-13775, doi:10.1021/acs.analchem.0c02008 (2020).

9 Dallmann, R., Viola, A. U., Tarokh, L., Cajochen, C. & Brown, S. A. The human circadian metabolome. *P Natl Acad Sci USA* **109**, 2625-2629, doi:10.1073/pnas.1114410109 (2012).

10 Zhang, J. J. *et al.* Nuclear dihydroxyacetone phosphate signals nutrient sufficiency and cell cycle phase to global histone acetylation. *Nat Metab* **3**, 859-875, doi:10.1038/s42255-021-00405-8 (2021).

11 Paik, W. K., Bloch-Frankenthal, L., Birnbaum, S. M., Winitz, M. & Greenstein, J. P. ϵ-Lysine acylase. *Arch Biochem Biophys* **69**, 56-66, doi:10.1016/0003-9861(57)90472-1 (1957).

12 Neumann, H., Peak-Chew, S. Y. & Chin, J. W. Genetically encoding N-epsilon-acetyllysine in recombinant proteins. *Nat Chem Biol* **4**, 232-234, doi:DOI 10.1038/nchembio.73 (2008).

13 Guo, M., Ignatov, M., Musier-Forsyth, K., Schimmel, P. & Yang, X. L. Crystal structure of tetrameric form of human lysyl-tRNA synthetase: Implications for multisynthetase complex formation. *P Natl Acad Sci USA* **105**, 2331-2336, doi:10.1073/pnas.0712072105 (2008).

14 He, X. D. *et al.* Sensing and Transmitting Intracellular Amino Acid Signals through Reversible Lysine Aminoacylations. *Cell Metab* **27**, 151-+, doi:10.1016/j.cmet.2017.10.015 (2018).

15 Yanagisawa, T., Sumida, T., Ishii, R., Takemoto, C. & Yokoyama, S. A paralog of lysyl-tRNA synthetase aminoacylates a conserved lysine residue in translation elongation factor P. *Nat Struct Mol Biol* **17**, 1136-U1114, doi:10.1038/nsmb.1889 (2010).

16 Ling, J., Reynolds, N. & Ibba, M. Aminoacyl-tRNA synthesis and translational quality control. *Annu Rev Microbiol* **63**, 61-78, doi:10.1146/annurev.micro.091208.073210 (2009).

17 Guo, Y., Li, D. F., Ji, H. N., Zheng, J. T. & Zhou, N. Y. Hexachlorobenzene Monooxygenase Substrate Selectivity and Catalysis: Structural and Biochemical Insights. *Appl Environ Microb* **87**, doi:ARTN e01965-2010.1128/AEM.01965-20 (2021).

18 Desogus, G., Todone, F., Brick, P. & Onesti, S. Active site of lysyl-tRNA synthetase: Structural studies of the adenylation reaction. *Biochemistry-Us* **39**, 8418-8425, doi:10.1021/bi0006722 (2000).

19 Wolfson, N. A., Pitcairn, C. A., Sullivan, E. D., Joseph, C. G. & Fierke, C. A. An enzyme-

coupled assay measuring acetate production for profiling histone deacetylase specificity. *Anal Biochem* **456**, 61-69, doi:10.1016/j.ab.2014.03.012 (2014).
20 Fujino, T., Kondo, J., Ishikawa, M., Morikawa, K. & Yamamoto, T. T. Acetyl-CoA synthetase 2, a mitochondrial matrix enzyme involved in the oxidation of acetate. *J Biol Chem* **276**, 11420-11426, doi:DOI 10.1074/jbc.M008782200 (2001).
21 Luong, A., Hannah, V. C., Brown, M. S. & Goldstein, J. L. Molecular characterization of human acetyl-CoA synthetase, an enzyme regulated by sterol regulatory element-binding proteins. *J Biol Chem* **275**, 26458-26466, doi:DOI 10.1074/jbc.M004160200 (2000).
22 Drazic, A., Myklebust, L. M., Ree, R. & Arnesen, T. The world of protein acetylation. *Bba-Proteins Proteom* **1864**, 1372-1401, doi:10.1016/j.bbapap.2016.06.007 (2016).
23 Narita, T., Weinert, B. T. & Choudhary, C. Functions and mechanisms of non-histone protein acetylation. *Nat Rev Mol Cell Bio* **20**, 156-174, doi:10.1038/s41580-018-0081-3 (2019).
24 Sabari, B. R., Zhang, D., Allis, C. D. & Zhao, Y. M. Metabolic regulation of gene expression through histone acylations. *Nat Rev Mol Cell Bio* **18**, 90-101, doi:10.1038/nrm.2016.140 (2017).
25 Gromiha, M. M. & Selvaraj, S. Inter-residue interactions in protein folding and stability. *Prog Biophys Mol Bio* **86**, 235-277, doi:10.1016/j.pbiomolbio.2003.09.003 (2004).
26 Xiaoyan Zhang, Z. O. Crystal structure of aldehyde dehydrogenase 1A1 from mouse. *Biochem Bioph Res Co*, doi:https://doi.org/10.1016/j.bbrc.2022.08.054 (2022).
27 Baeza, J. *et al.* Stoichiometry of Site-specific Lysine Acetylation in an Entire Proteome. *J Biol Chem* **289**, 21326-21338, doi:10.1074/jbc.M114.581843 (2014).
28 Mune Mune, M. A., Minka, S. R. & Mbome, I. L. Functional properties of acetylated and succinylated cowpea protein concentrate and effect of enzymatic hydrolysis on solubility. *International journal of food sciences and nutrition* **62**, 310-317, doi:10.3109/09637486.2010.538670 (2011).
29 Itoh, M. *et al.* Biallelic KARS pathogenic variants cause an early-onset progressive leukodystrophy. *Brain : a journal of neurology* **142**, 560-573, doi:10.1093/brain/awz001 (2019).
30 Wang, F. *et al.* Targeted inhibition of mutant IDH2 in leukemia cells induces cellular differentiation. *Science (New York, N.Y.)* **340**, 622-626, doi:10.1126/science.1234769 (2013).
31 Kabsch, W. Integration, scaling, space-group assignment and post-refinement. *Acta Crystallographica Section D-Biological Crystallography* **66**, 133-144, doi:10.1107/S0907444909047374 (2010).
32 Adams, P. D. *et al.* PHENIX: a comprehensive Python-based system for macromolecular structure solution. *Acta Crystallogr D* **66**, 213-221, doi:10.1107/S0907444909052925 (2010).
33 Emsley, P., Lohkamp, B., Scott, W. G. & Cowtan, K. Features and development of Coot. *Acta Crystallographica Section D-Biological Crystallography* **66**, 486-501, doi:10.1107/S0907444910007493 (2010).
34 Afonine, P. V. *et al.* Towards automated crystallographic structure refinement with phenix.refine. *Acta Crystallogr D* **68**, 352-367, doi:10.1107/S0907444912001308 (2012).
35 Chen, V. B. *et al.* MolProbity: all-atom structure validation for macromolecular crystallography. *Acta crystallographica. Section D, Biological crystallography* **66**, 12-21, doi:10.1107/s0907444909042073 (2010).
36 Liu, Y. *et al.* CB-Dock: a web server for cavity detection-guided protein-ligand blind docking. *Acta pharmacologica Sinica* **41**, 138-144, doi:10.1038/s41401-019-0228-6 (2020).
37 Wang, Y. *et al.* KAT2A coupled with the α-KGDH complex acts as a histone H3

succinyltransferase. *Nature* **552**, 273-277, doi:10.1038/nature25003 (2017).
38 Janssen, B. D., Diner, E. J. & Hayes, C. S. Analysis of aminoacyl- and peptidyl-tRNAs by gel electrophoresis. *Methods in molecular biology (Clifton, N.J.)* **905**, 291-309, doi:10.1007/978-1-61779-949-5_19 (2012).
39 Merico, D., Isserlin, R., Stueker, O., Emili, A. & Bader, G. D. Enrichment map: a network-based method for gene-set enrichment visualization and interpretation. *PloS one* **5**, e13984, doi:10.1371/journal.pone.0013984 (2010).
40 Shannon, P. *et al.* Cytoscape: a software environment for integrated models of biomolecular interaction networks. *Genome research* **13**, 2498-2504, doi:10.1101/gr.1239303 (2003).

Figure 1

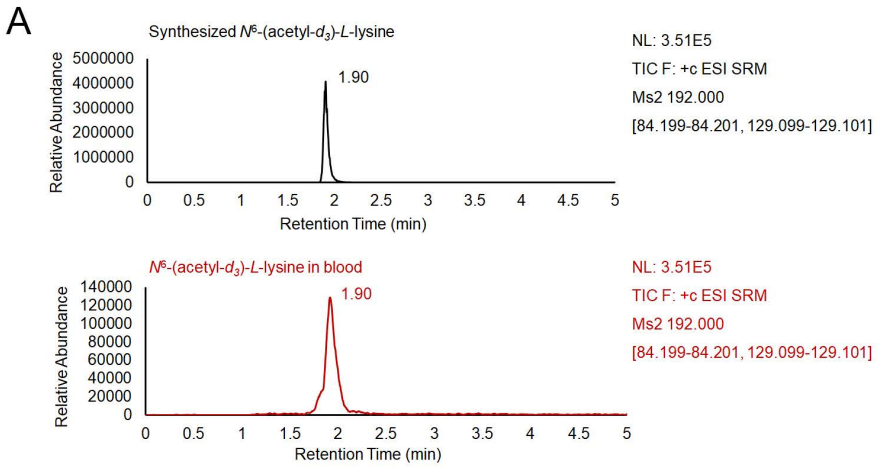

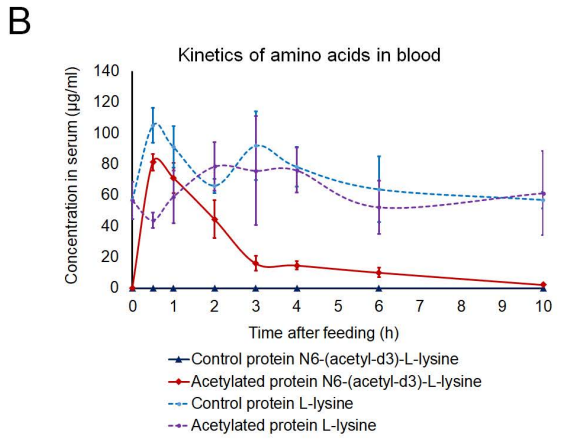

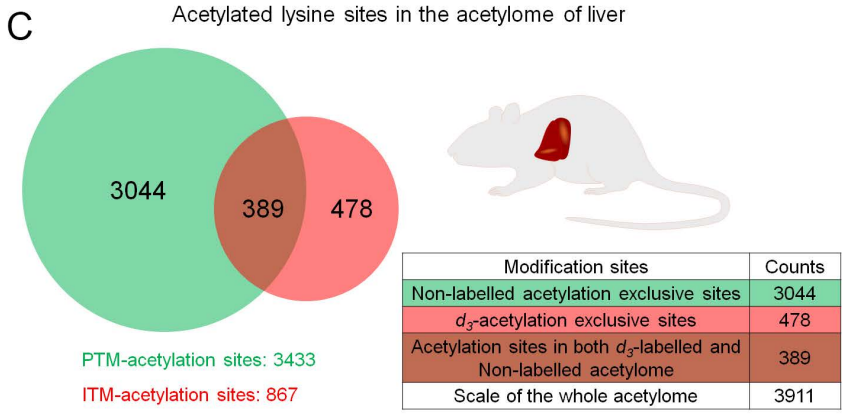

Modification sites	Counts
Non-labelled acetylation exclusive sites	3044
d_3-acetylation exclusive sites	478
Acetylation sites in both d_3-labelled and Non-labelled acetylome	389
Scale of the whole acetylome	3911

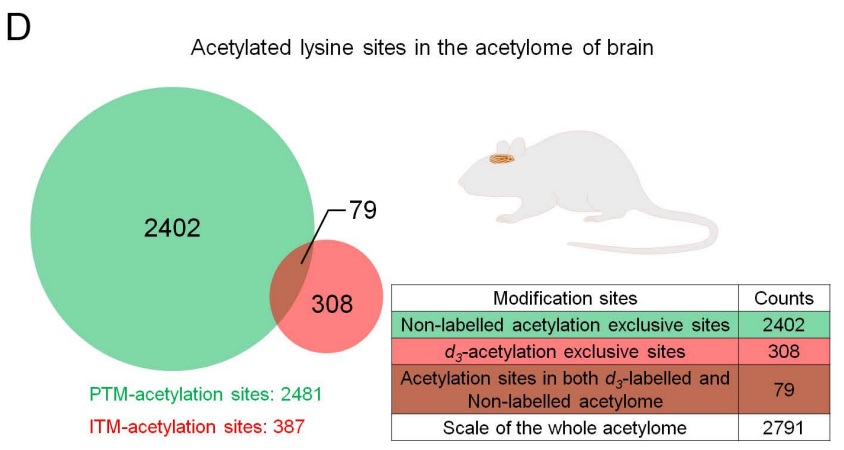

Modification sites	Counts
Non-labelled acetylation exclusive sites	2402
d_3-acetylation exclusive sites	308
Acetylation sites in both d_3-labelled and Non-labelled acetylome	79
Scale of the whole acetylome	2791

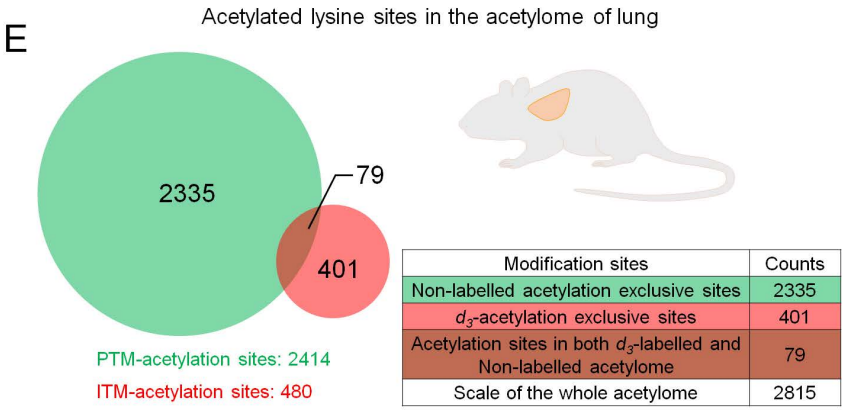

Modification sites	Counts
Non-labelled acetylation exclusive sites	2335
d_3-acetylation exclusive sites	401
Acetylation sites in both d_3-labelled and Non-labelled acetylome	79
Scale of the whole acetylome	2815

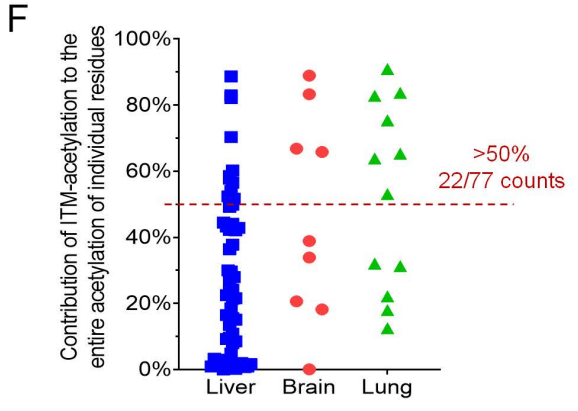

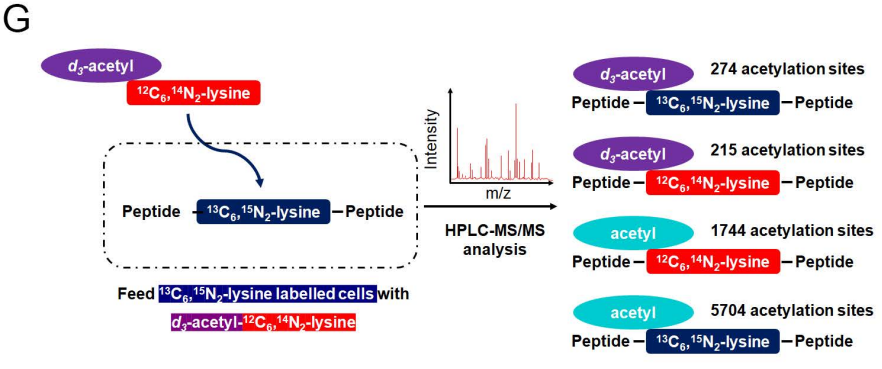

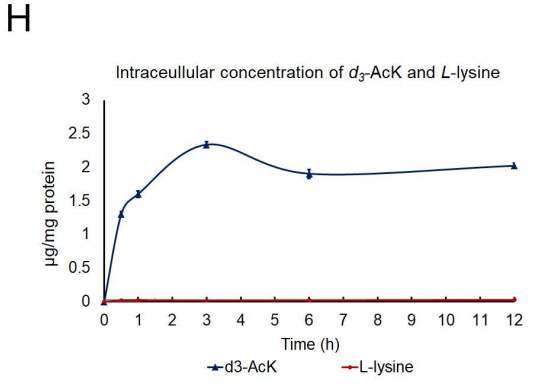

Figure 2

A

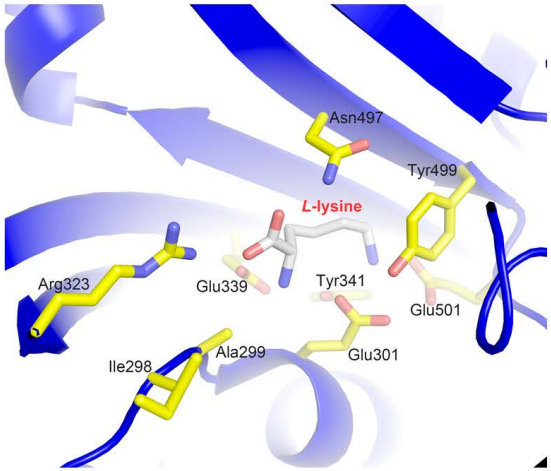

B

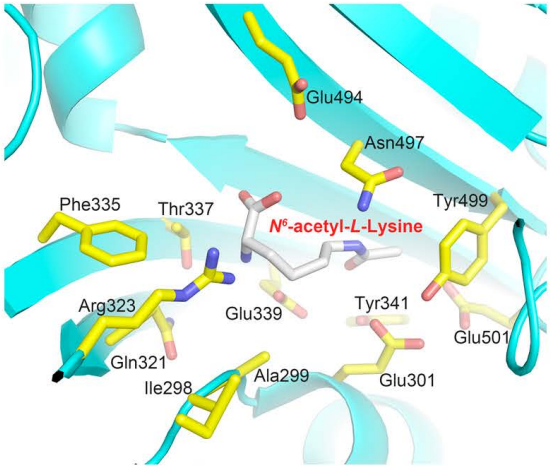

C

Interacting Residues	
Lysine	Nε-acetyl-lysine
Ile298	Ile298
Ala299	Ala299
Glu301	Glu301
	Gln321
Arg323	Arg323
	Phe335
	Thr337
Glu339	Glu339
Tyr341	Tyr341
	Glu494
Asn497	Asn497
Tyr499	Tyr499
Glu501	Glu501

D

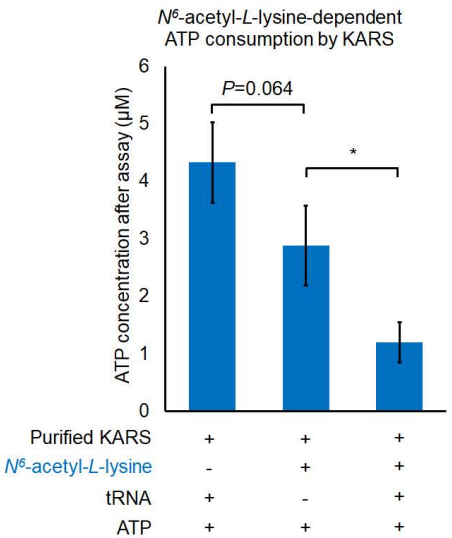

E

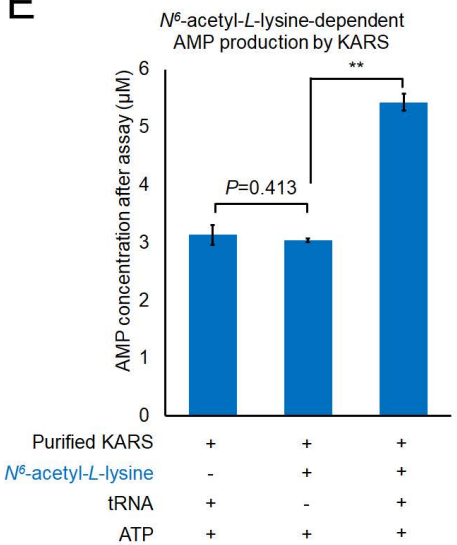

F

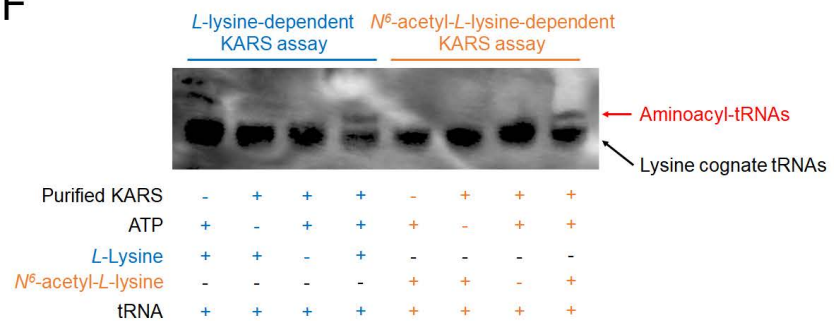

Figure 3

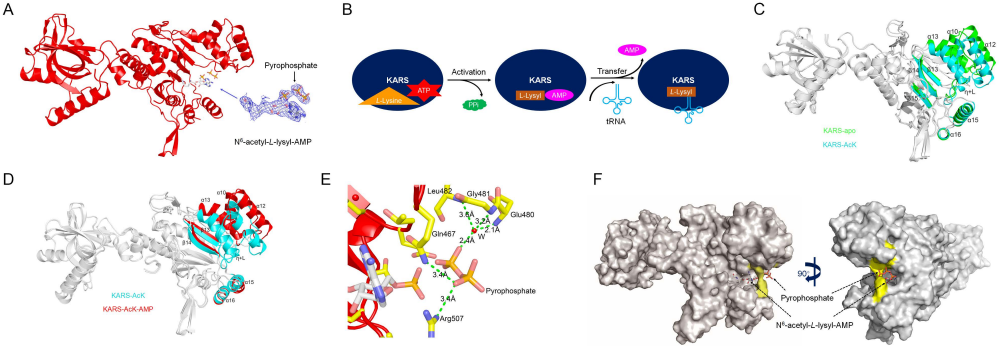
A
Pyrophosphate
Nε-acetyl-L-lysyl-AMP
B
KARS
ATP
L-Lysine
Activation
PPi
KARS
L-Lysyl
AMP
Transfer
AMP
tRNA
KARS
L-Lysyl
C
KARS-apo
KARS-AcK
D
KARS-AcK
KARS-AcK-AMP
E
Leu482
Gly481
Glu480
Gln467
Arg507
Pyrophosphate
F
90°
Pyrophosphate
Nε-acetyl-L-lysyl-AMP

Figure 4

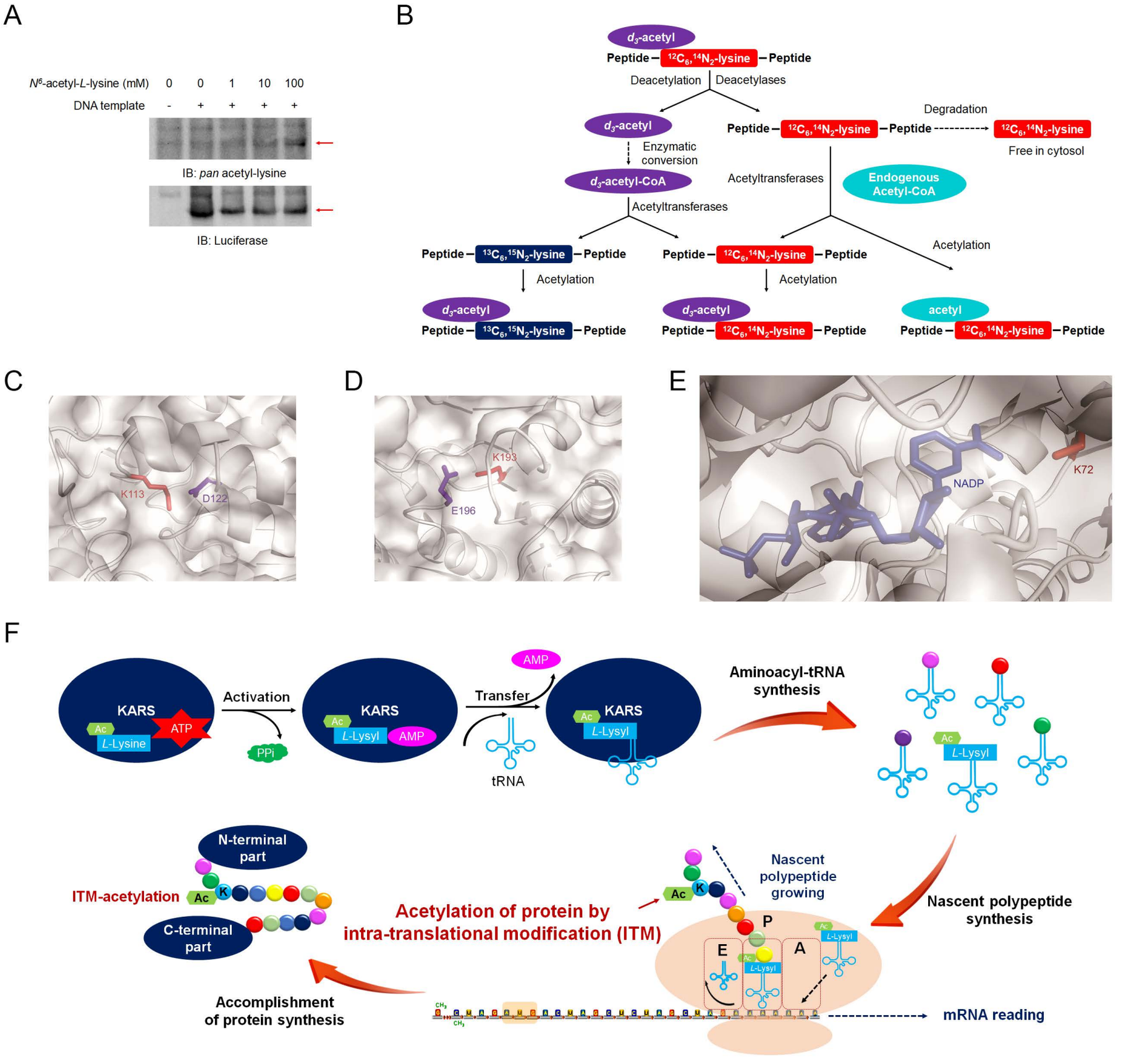
A
N6-acetyl-L-lysine (mM) 0 0 1 10 100
DNA template - + + + +
IB: pan acetyl-lysine
IB: Luciferase
B
d3-acetyl
Peptide – 12C6,14N2-lysine – Peptide
Deacetylation
Deacetylases
Degradation
Peptide – 12C6,14N2-lysine – Peptide
12C6,14N2-lysine
Free in cytosol
Enzymatic conversion
d3-acetyl-CoA
Acetyltransferases
Endogenous Acetyl-CoA
Acetyltransferases
Acetylation
Peptide – 13C6,15N2-lysine – Peptide
Peptide – 12C6,14N2-lysine – Peptide
Acetylation
Acetylation
d3-acetyl
Peptide – 13C6,15N2-lysine – Peptide
d3-acetyl
Peptide – 12C6,14N2-lysine – Peptide
acetyl
Peptide – 12C6,14N2-lysine – Peptide
C
K113
D122
D
K193
E196
E
NADP
K72
F
KARS
Ac
L-Lysine
ATP
Activation
PPi
KARS
Ac
L-Lysyl
AMP
Transfer
AMP
tRNA
KARS
Ac
L-Lysyl
Aminoacyl-tRNA synthesis
Ac
L-Lysyl
Nascent polypeptide synthesis
Nascent polypeptide growing
Ac
K
P
E
A
Ac
L-Lysyl
Ac
L-Lysyl
Acetylation of protein by intra-translational modification (ITM)
N-terminal part
ITM-acetylation
Ac
K
C-terminal part
Accomplishment of protein synthesis
mRNA reading

Figure S1

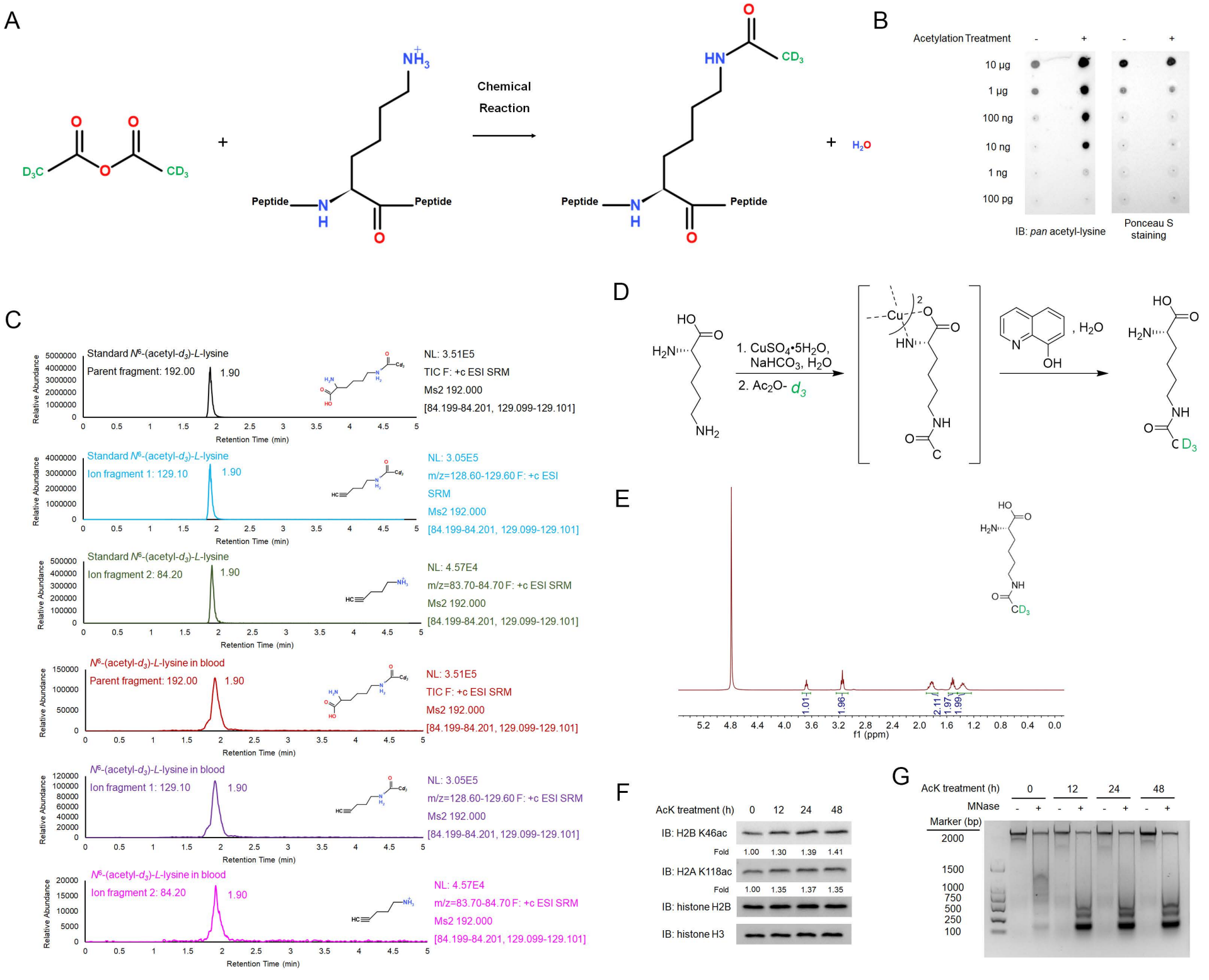
A
Chemical Reaction
Peptide
Peptide
B
Acetylation Treatment
10 μg
1 μg
100 ng
10 ng
1 ng
100 pg
IB: pan acetyl-lysine
Ponceau S staining
C
Standard N6-(acetyl-d3)-L-lysine
Parent fragment: 192.00
Ion fragment 1: 129.10
Ion fragment 2: 84.20
N6-(acetyl-d3)-L-lysine in blood
Relative Abundance
Retention Time (min)
NL: 3.51E5
TIC F: +c ESI SRM
NL: 3.05E5
m/z=128.60-129.60 F: +c ESI SRM
NL: 4.57E4
m/z=83.70-84.70 F: +c ESI SRM
Ms2 192.000
[84.199-84.201, 129.099-129.101]
D
1. CuSO4•5H2O, NaHCO3, H2O
2. Ac2O- d3
E
f1 (ppm)
F
AcK treatment (h)
IB: H2B K46ac
Fold
IB: H2A K118ac
IB: histone H2B
IB: histone H3
G
AcK treatment (h)
MNase
Marker (bp)

Figure S2

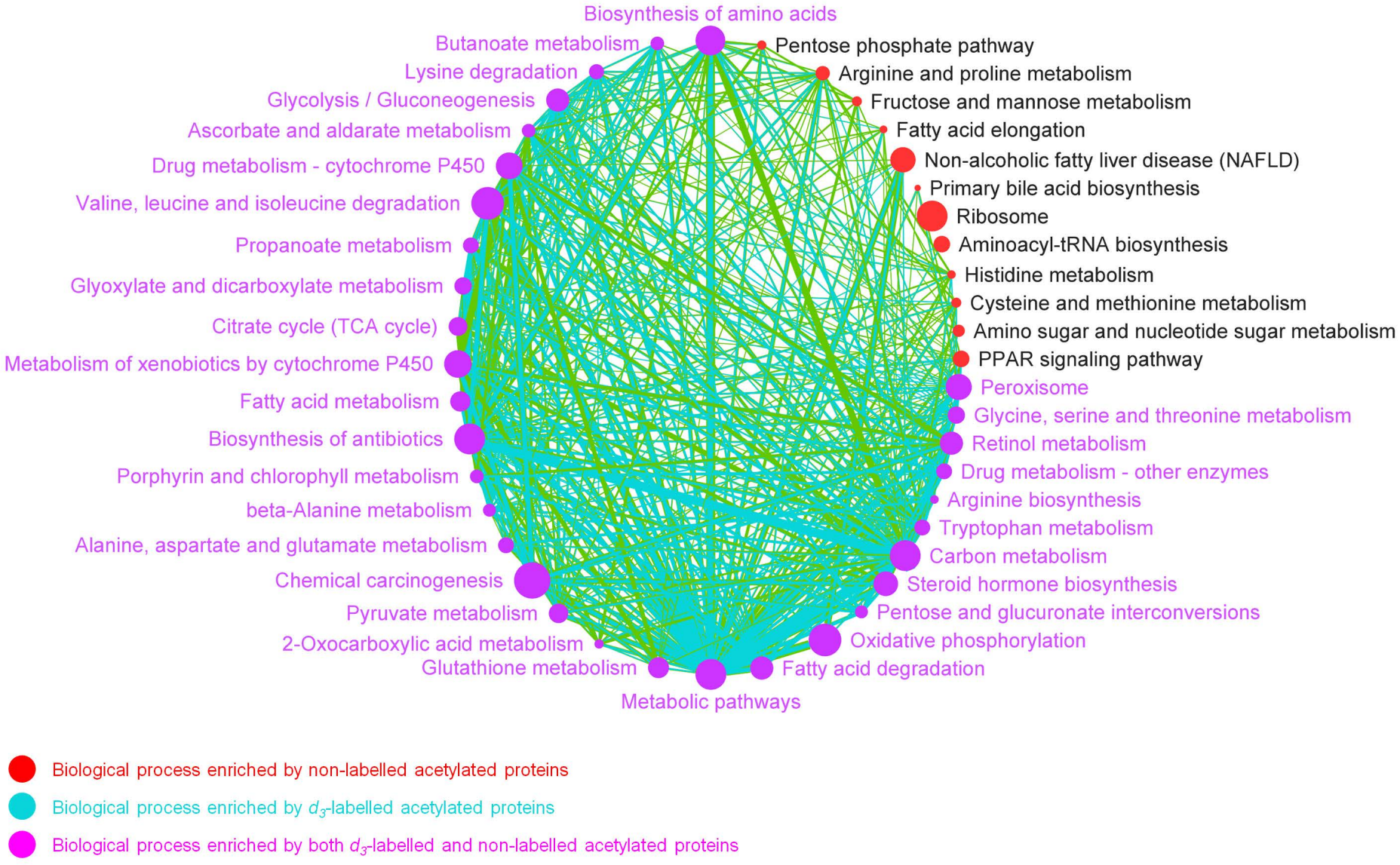
Biosynthesis of amino acids
Butanoate metabolism
Lysine degradation
Glycolysis / Gluconeogenesis
Ascorbate and aldarate metabolism
Drug metabolism - cytochrome P450
Valine, leucine and isoleucine degradation
Propanoate metabolism
Glyoxylate and dicarboxylate metabolism
Citrate cycle (TCA cycle)
Metabolism of xenobiotics by cytochrome P450
Fatty acid metabolism
Biosynthesis of antibiotics
Porphyrin and chlorophyll metabolism
beta-Alanine metabolism
Alanine, aspartate and glutamate metabolism
Chemical carcinogenesis
Pyruvate metabolism
2-Oxocarboxylic acid metabolism
Glutathione metabolism
Metabolic pathways
Fatty acid degradation
Oxidative phosphorylation
Pentose and glucuronate interconversions
Steroid hormone biosynthesis
Carbon metabolism
Tryptophan metabolism
Arginine biosynthesis
Drug metabolism - other enzymes
Retinol metabolism
Glycine, serine and threonine metabolism
Peroxisome
PPAR signaling pathway
Amino sugar and nucleotide sugar metabolism
Cysteine and methionine metabolism
Histidine metabolism
Aminoacyl-tRNA biosynthesis
Ribosome
Primary bile acid biosynthesis
Non-alcoholic fatty liver disease (NAFLD)
Fatty acid elongation
Fructose and mannose metabolism
Arginine and proline metabolism
Pentose phosphate pathway
Biological process enriched by non-labelled acetylated proteins
Biological process enriched by d_3-labelled acetylated proteins
Biological process enriched by both d_3-labelled and non-labelled acetylated proteins

Figure S3

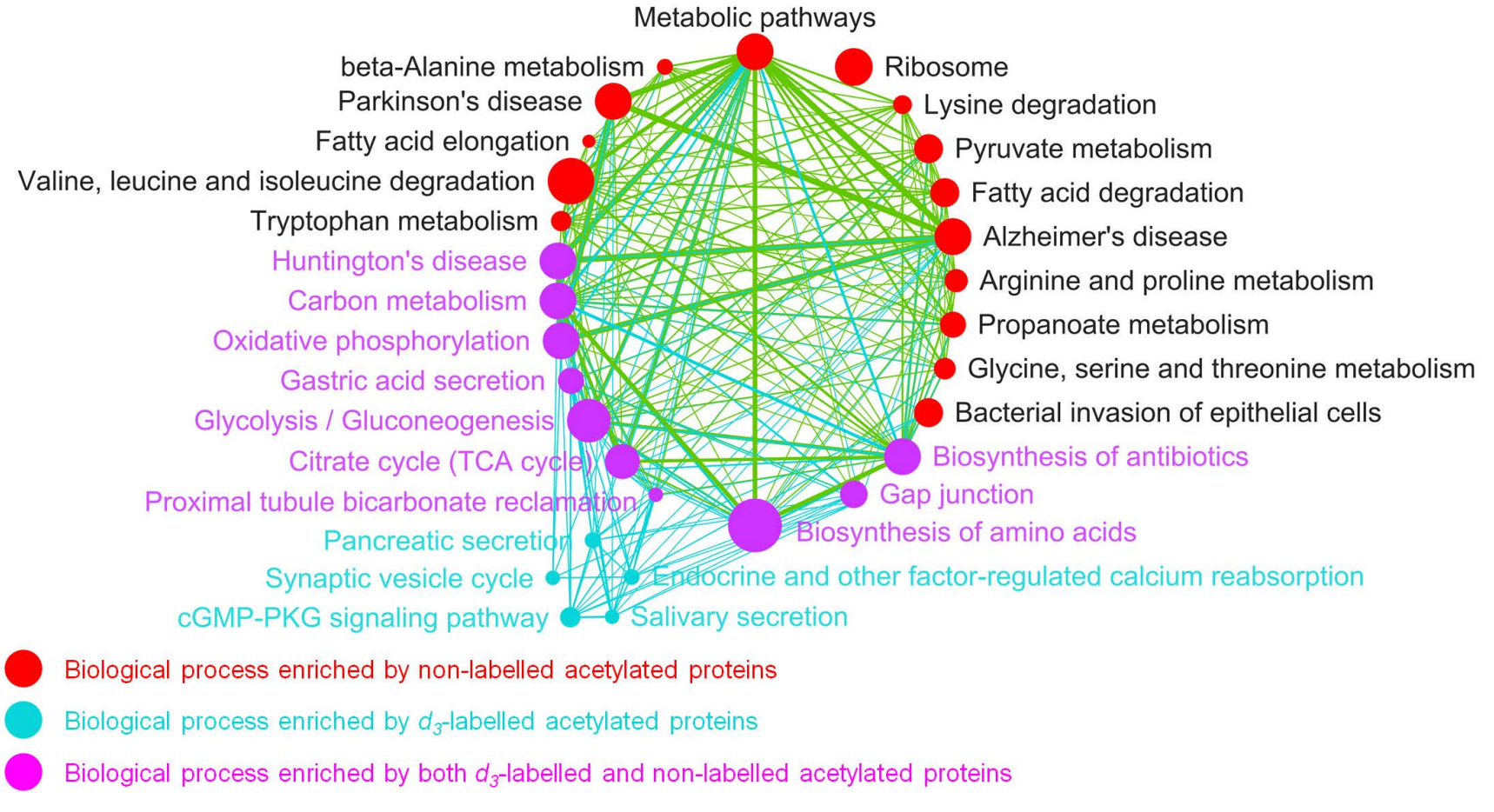
Metabolic pathways
beta-Alanine metabolism
Parkinson's disease
Fatty acid elongation
Valine, leucine and isoleucine degradation
Tryptophan metabolism
Huntington's disease
Carbon metabolism
Oxidative phosphorylation
Gastric acid secretion
Glycolysis / Gluconeogenesis
Citrate cycle (TCA cycle)
Proximal tubule bicarbonate reclamation
Pancreatic secretion
Synaptic vesicle cycle
cGMP-PKG signaling pathway
Ribosome
Lysine degradation
Pyruvate metabolism
Fatty acid degradation
Alzheimer's disease
Arginine and proline metabolism
Propanoate metabolism
Glycine, serine and threonine metabolism
Bacterial invasion of epithelial cells
Biosynthesis of antibiotics
Gap junction
Biosynthesis of amino acids
Endocrine and other factor-regulated calcium reabsorption
Salivary secretion
Biological process enriched by non-labelled acetylated proteins
Biological process enriched by d_3-labelled acetylated proteins
Biological process enriched by both d_3-labelled and non-labelled acetylated proteins

Figure S4

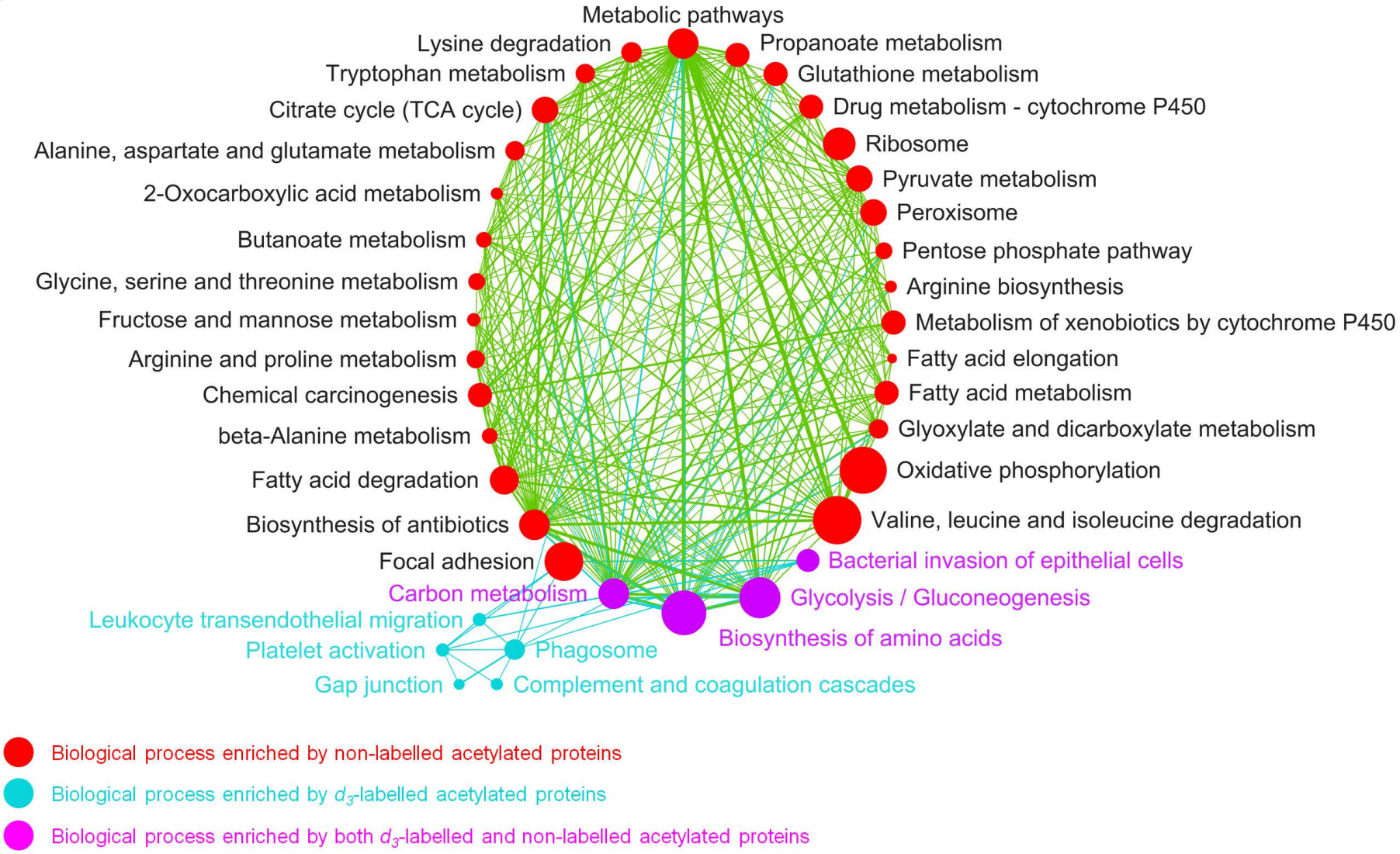
Metabolic pathways
Lysine degradation
Propanoate metabolism
Tryptophan metabolism
Glutathione metabolism
Citrate cycle (TCA cycle)
Drug metabolism - cytochrome P450
Alanine, aspartate and glutamate metabolism
Ribosome
2-Oxocarboxylic acid metabolism
Pyruvate metabolism
Peroxisome
Butanoate metabolism
Pentose phosphate pathway
Glycine, serine and threonine metabolism
Arginine biosynthesis
Fructose and mannose metabolism
Metabolism of xenobiotics by cytochrome P450
Arginine and proline metabolism
Fatty acid elongation
Chemical carcinogenesis
Fatty acid metabolism
beta-Alanine metabolism
Glyoxylate and dicarboxylate metabolism
Fatty acid degradation
Oxidative phosphorylation
Biosynthesis of antibiotics
Valine, leucine and isoleucine degradation
Focal adhesion
Bacterial invasion of epithelial cells
Carbon metabolism
Glycolysis / Gluconeogenesis
Leukocyte transendothelial migration
Biosynthesis of amino acids
Platelet activation
Phagosome
Gap junction
Complement and coagulation cascades
Biological process enriched by non-labelled acetylated proteins
Biological process enriched by d_3-labelled acetylated proteins
Biological process enriched by both d_3-labelled and non-labelled acetylated proteins

Figure S5

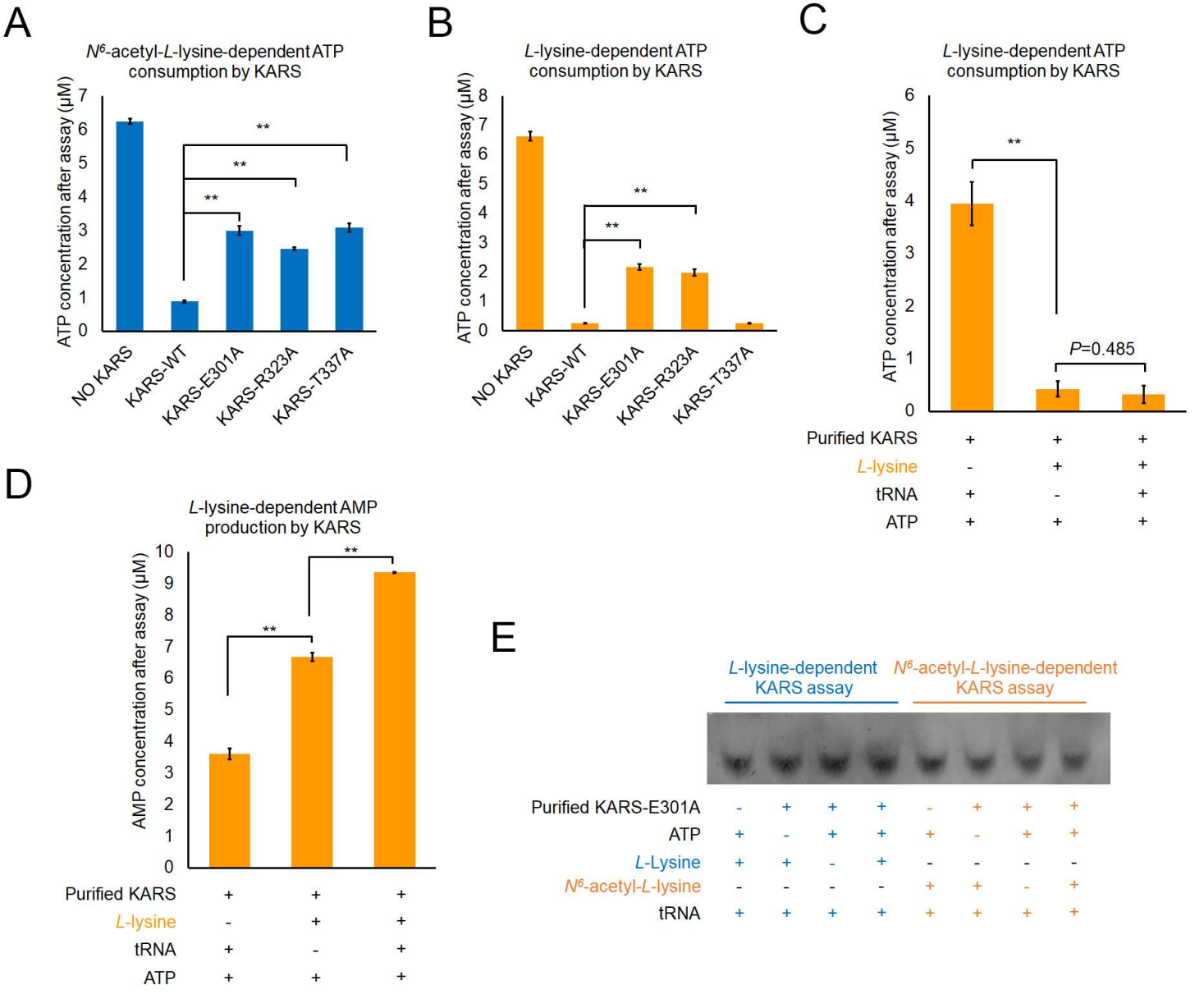
A
N6-acetyl-L-lysine-dependent ATP consumption by KARS
ATP concentration after assay (μM)
0
1
2
3
4
5
6
7
**
**
**
NO KARS
KARS-WT
KARS-E301A
KARS-R323A
KARS-T337A
B
L-lysine-dependent ATP consumption by KARS
ATP concentration after assay (μM)
0
1
2
3
4
5
6
7
8
**
**
NO KARS
KARS-WT
KARS-E301A
KARS-R323A
KARS-T337A
C
L-lysine-dependent ATP consumption by KARS
ATP concentration after assay (μM)
0
1
2
3
4
5
6
**
P=0.485
Purified KARS + + +
L-lysine - + +
tRNA + - +
ATP + + +
D
L-lysine-dependent AMP production by KARS
AMP concentration after assay (μM)
0
1
2
3
4
5
6
7
8
9
10
**
**
Purified KARS + + +
L-lysine - + +
tRNA + - +
ATP + + +
E
L-lysine-dependent KARS assay
N6-acetyl-L-lysine-dependent KARS assay
Purified KARS-E301A - + + + - + + +
ATP + - + + + - + +
L-Lysine + + - + - - - -
N6-acetyl-L-lysine - - - - + + - +
tRNA + + + + + + + +

Figure S6

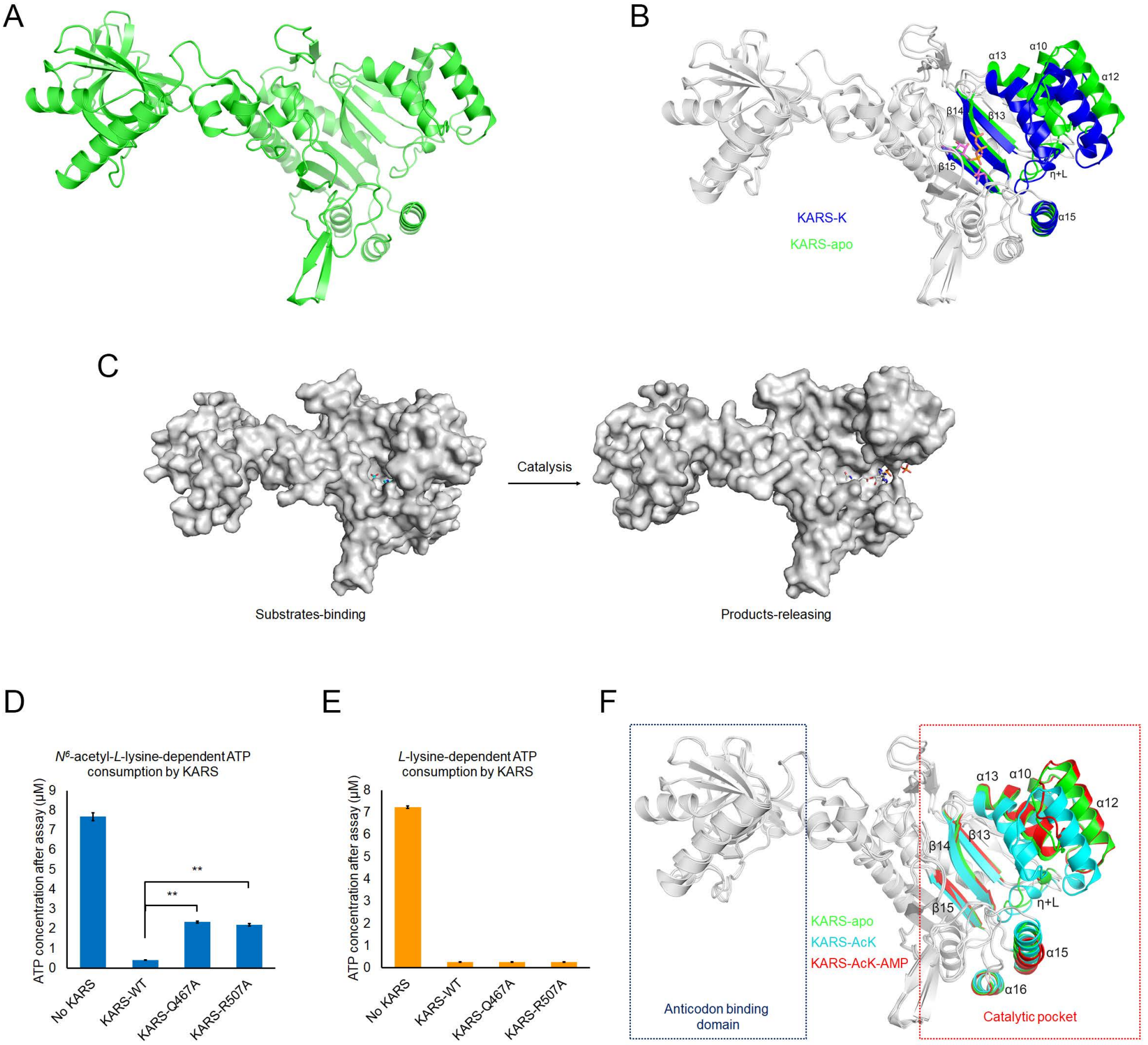
A
B
α13
α10
α12
β14
β13
β15
η+L
α15
KARS-K
KARS-apo
C
Catalysis
Substrates-binding
Products-releasing
D
N6-acetyl-L-lysine-dependent ATP consumption by KARS
ATP concentration after assay (μM)
0
1
2
3
4
5
6
7
8
9
**
**
No KARS
KARS-WT
KARS-Q467A
KARS-R507A
E
L-lysine-dependent ATP consumption by KARS
ATP concentration after assay (μM)
0
1
2
3
4
5
6
7
8
No KARS
KARS-WT
KARS-Q467A
KARS-R507A
F
α13
α10
α12
β14
β13
β15
η+L
α15
α16
KARS-apo
KARS-AcK
KARS-AcK-AMP
Anticodon binding domain
Catalytic pocket

Figure S7

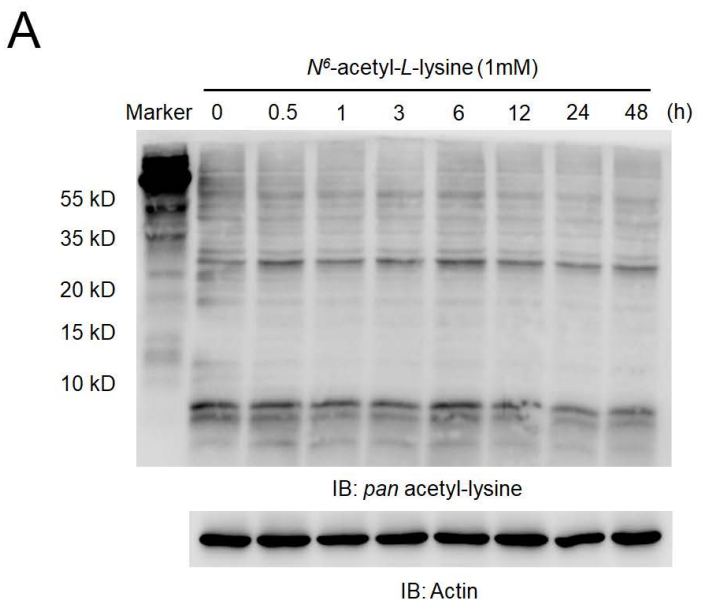
A
N^6-acetyl-*L*-lysine (1mM)
Marker 0 0.5 1 3 6 12 24 48 (h)
55 kD
35 kD
20 kD
15 kD
10 kD
IB: *pan* acetyl-lysine
IB: Actin

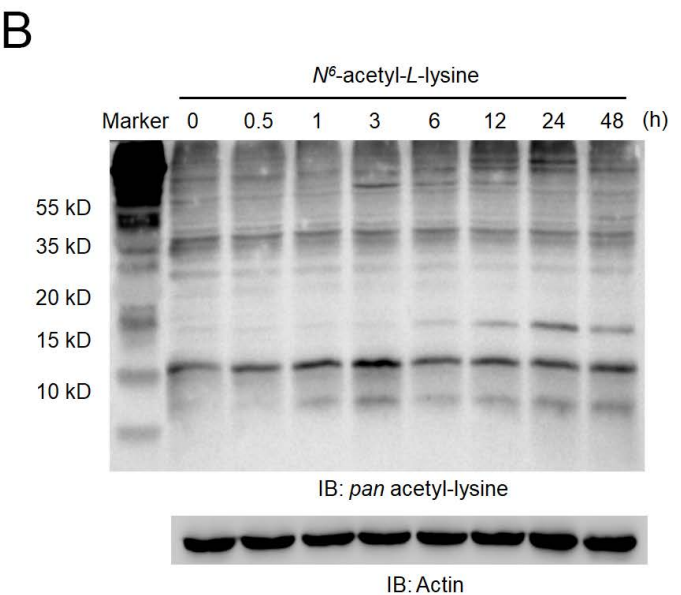
B
N^6-acetyl-*L*-lysine
Marker 0 0.5 1 3 6 12 24 48 (h)
55 kD
35 kD
20 kD
15 kD
10 kD
IB: *pan* acetyl-lysine
IB: Actin

Figure S8

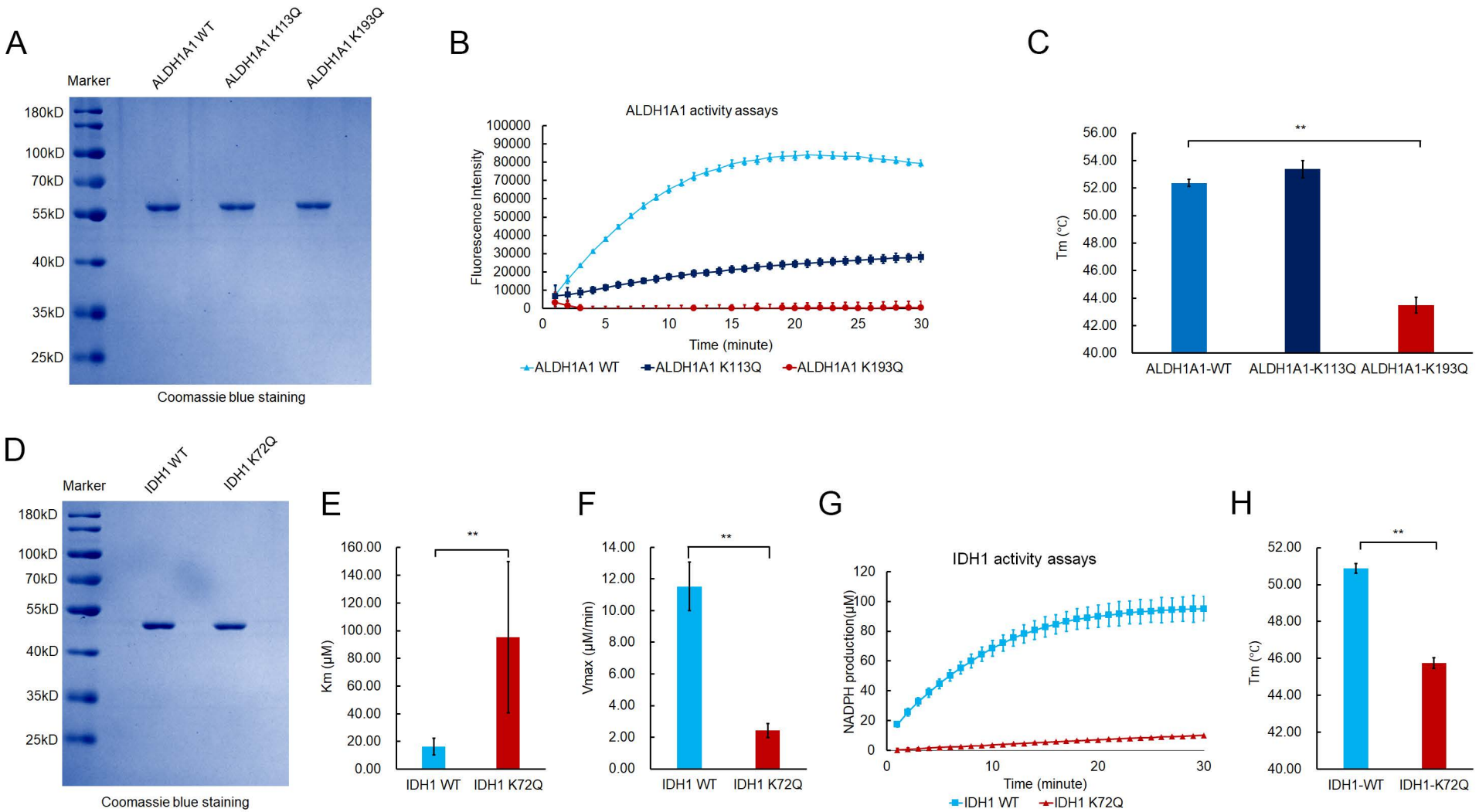
A
Marker
ALDH1A1 WT
ALDH1A1 K113Q
ALDH1A1 K193Q
180kD
100kD
70kD
55kD
40kD
35kD
25kD
Coomassie blue staining
B
ALDH1A1 activity assays
Fluorescence Intensity
Time (minute)
ALDH1A1 WT
ALDH1A1 K113Q
ALDH1A1 K193Q
C
Tm (°C)
**
ALDH1A1-WT
ALDH1A1-K113Q
ALDH1A1-K193Q
D
Marker
IDH1 WT
IDH1 K72Q
180kD
100kD
70kD
55kD
40kD
35kD
25kD
Coomassie blue staining
E
Km (μM)
**
IDH1 WT
IDH1 K72Q
F
Vmax (μM/min)
**
IDH1 WT
IDH1 K72Q
G
IDH1 activity assays
NADPH production(μM)
Time (minute)
IDH1 WT
IDH1 K72Q
H
Tm (°C)
**
IDH1-WT
IDH1-K72Q